OVERLOAD AND VARIABLE AMPLITUDE LOAD EFFECTS ON THE FATIGUE STRENGTH OF WELDED JOINTS

Ylikuorman sekä vaihtuva-amplitudisen kuormituksen vaikutus hitsattujen liitosten väsymislujuuteen

ABSTRACT

Lappeenranta–Lahti University of Technology LUT

LUT School of Energy Systems

LUT Mechanical Engineering

Kiia Grönlund

Overload and variable amplitude load effects on the fatigue strength of welded joints

Master's thesis

2023

78 pages, 56 figures, 11 tables and 6 appendices

Examiners: Professor Timo Björk and Antti Ahola, D.Sc. (Tech.)

Keywords: Overload, fatigue strength, welded joints, 4R method, variable amplitude load

In this thesis, overload and variable amplitude load effects on the fatigue strength of welded joints are studied using both experimental and analytical methods. The main methods of the study are fatigue testing of welded structures and analytical calculations using the effective notch stress method with the novel 4R notch stress approach. Residual stress measurements are also included in the experimental testing. The effect of the overload is studied by applying a tensile overload on the welded joint before fatigue testing. The overloads are tested on two levels 60 % and 80 % of the nominal yield strength. Variable amplitude loading is tested with Gaussian load spectrum consisting of a high peak load and following decreasing cycles.

The joint type under examination is a welded non-load carrying longitudinal joint with double-sided gussets. The main material in the study is structural steel S700. Steel grades S355 and S1100 are acting as a control group for the overload cases to evaluate the possible differences or correlation in the results. A total of 39 fatigue tests are conducted in this thesis.

The results indicated that the overload relaxes the residual stresses and therefore increases the fatigue strength of welded joints. The higher-level overload had a more notable effect on the results in comparison with the lower one. In the case of steel grade S700, overload of 0.8 yield strength resulted in 1.6 times higher mean fatigue strength. It was also noted that steel grade S1100 gained benefit most from the pre-applied overload and steel grade S355 the least.

The application of the 4R method to overload and variable amplitude load cases was also evaluated. The 4R method was able to conduct mean stress correction and more accurately estimated the fatigue strength of welded structures under overload and variable amplitude loading with respect to traditional methods.

TIIVISTELMÄ

Lappeenrannan–Lahden teknillinen yliopisto LUT

LUT Energiajärjestelmät

LUT Konetekniikka

Kiia Grönlund

Ylikuorman sekä vaihtuva-amplitudisen kuormituksen vaikutus hitsattujen liitosten väsymislujuuteen

Diplomityö

2023

78 sivua, 56 kuvaa, 11 taulukkoa ja 6 liitettä

Tarkastajat: Professori Timo Björk ja Antti Ahola, TkT

Avainsanat: Ylikuorma, väsymislujuus, hitsatut liitokset, 4R-menetelmä, vaihtuva amplitudinen kuormitus

Tämän työn tavoitteena on tutkia ylikuorman sekä vaihtuva-amplitudisen kuormituksen vaikutusta hitsattujen liitosten väsymislujuuteen käyttäen kokeellista tutkimusta ja analyyttisia laskentamenetelmiä. Laskennan pääpaino on 4R-menetelmän soveltamisessa ylikuorma- ja vaihtuva-amplitudisiin kuormitustapauksiin. Kokeellinen tutkimus keskittyy väsymiskokeisiin sekä jäännösjännitysmittauksiin. Ylikuorman vaikutusta hitsattuihin liitoksiin tutkitaan staattisen vetokuorman avulla kahdella ylikuormitustasolla. Ylikuormat määritettiin olevan 60 % ja 80 % materiaalin nimellisestä myötölujuudesta. Vaihtuva-amplitudinen kuormitus sisälsi yksittäisen korkean piikkijännityksen sekä sarjan laskevia kuormitussyklejä.

Tutkittava liitostyyppi on kuormaa kantamaton pitkittäinen molemminpuolinen ripa ja työn päämateriaali rakenneteräs S700. Rakenneteräkset S355 ja S1100 toimivat vertailuryhmänä ylikuormatapauksille mahdollisen vastaavuuden selvittämiseksi. Työssä toteutettiin yhteensä 39 väsymiskoetta.

Tulokset viittasivat ylikuorman alentavan jäännösjännityksiä ja näin ollen parantavan hitsattujen liitosten väsymislujuutta. Korkein ylikuormataso nosti S700 teräslajin tapauksessa väsymislujuutta noin 1.6 kertaa korkeammaksi verrattuna vakioamplitudiseen kuormitukseen. Työssä huomattiin lisäksi teräslajin S1100 hyötyvän väsymislujuuden näkökulmasta eniten ylikuormituksesta ja S355 teräksen vähiten.

Työssä arvioitiin myös 4R-väsymislaskentamenetelmän soveltuvuutta ylikuorma- ja vaihtuva-amplitudisiin kuormitustapauksiin. 4R-menetelmässä toteutettava lokaali keskijännityskorjaus sekä jäännösjännitysten huomiointi mahdollisti ennusteiden paremman tarkkuuden sekä vastaavuuden verrattuna perinteisiin väsymislaskentamenetelmiin.

ACKNOWLEDGEMENTS

Last but not least, many thanks and warmest wishes to my family who have encouraged me and been my strength during these studies.

Kiia Grönlund

In Lappeenranta, 16th of May 2023

SYMBOLS AND ABBREVIATIONS

Roman characters

A_5	elongation	[%]
C_{4R}	fatigue capacity	[-]
D	damage sum	[-]
E	elastic modulus	[GPa]
F_2	shape factor	[-]
FAT_{char}	mean fatigue class	[MPa]
FAT_{mean}	characteristic fatigue class	[MPa]
H	strain hardening coefficient	[MPa]
H_i	Load spectrum	[-]
H_0	Length of a block	[-]
I	current	[A]
K_m	membrane stress concentration	[-]
K_b	bending stress concentration	[-]
L	critical length	[mm]
m	slope of the S-N curve	[-]
$N_{f,4R}$	fatigue life	[-]
n	strain hardening exponent	[-]
p	scaling factor for VA loads	[-]
Q_{avg}	average heat input	[kJ/mm]
R	externally applied stress ratio	[-]
R_{local}	local stress concentration	[-]

R_m	ultimate strength of the material	[MPa]
$R_{p,0.2}$	offset yield strength	[MPa]
r_{true}	weld toe radius	[mm]
t	thickness	[mm]
$t_{8/5}$	cooling time (from 800 °C to 500 °C)	[s]
T_0	interpass temperature	[°C]
U	voltage	[V]
v_G	gaussian shape factor	[-]
v_t	travel speed	[m/min]
v_{wire}	wire feed speed rate	[m/min]

Greek characters

ε	total strain	[-]
ε_e	elastic strain	[-]
ε_p	plastic strain	[-]
ε_{sg}	strain from strain gage	[-]
$\Delta\sigma$	stress range	[MPa]
σ	stress	[MPa]
σ_{eff}	effective stress	[MPa]
$\Delta\sigma_{\text{eq}}$	equivalent stress range	[MPa]
σ_{HS}	hot-spot stress	[MPa]
σ_k	notch stress	[MPa]
$\Delta\sigma_k$	notch stress range	[MPa]
$\sigma_{k,\text{res}}$	local residual stress	[MPa]

$\sigma_{k,eq}$	equivalent notch stress range	[MPa]
σ_{max}	maximum nominal stress	[MPa]
σ_{min}	minimum nominal stress	[MPa]
$\sigma_{max,loc}$	maximum local stress	[MPa]
$\sigma_{min,loc}$	minimum local stress	[MPa]
$\Delta\sigma_{nom}$	nominal stress range	[MPa]
$\Delta\sigma_{nom,max}$	maximum nominal stress range	[MPa]
$\Delta\sigma_{nom,min}$	minimum nominal stress range	[MPa]
$\sigma(x)$	notch stress course	[MPa]
ρ	microstructural length	[mm]

Constants

v	Poisson's ratio	0.3

Abbreviations

AM	Area Method
CA	Constant Amplitude
ENS	Effective Notch Stress
FAT	Fatigue Classification
FEM	Finite Element Method
GMAW	Gas Metal Arc Welding
HFMI	High Frequency Impact Treatment
HS	Hot Spot Stress
IIW	International Institute of Welding

LM	Line Method
MSSPD	Minimization of Sum of Squared Perpendicular Distances
NLC	Non-Load Carrying
OL1	Overload level 1
OL2	Overload level 2
PM	Point Method
R-O	Ramberg-Osgood
4R	Novel Fatigue Assessment Method
S-N	Number of cycles to failure
SWT	Smith-Watson-Topper
TCD	Theory of Critical Distances
VA	Variable Amplitude
VM	Volume Method
YS	Yield strength

Table of contents

Abstract

Tiivistelmä

Acknowledgements

Symbols and abbreviations

Appendices

Appendix I: Welding procedure specifications

Appendix II: Welding parameters

Appendix III: Complete test matrixes with fatigue test results

Appendix IV: Measured strain values

Appendix V: Residual stress measurements of steel grade S700

Appendix VI: Polished cross-sections and macro figures with hardness measurements

1 Introduction

Fatigue of steel structures is among the main reasons for failure as multiple different components are subjected to cyclic load conditions in their use (Nussbaumer, Borges & Davaine 2018, p. 1; Carpinteri, Spagnoli & Vantadori 2017, p. 1010). Fatigue can occur when cyclic loading is applied to a structure repeatedly. This cyclic loading can then lead to propagating cracks and damage. (Nussbaumer et al. 2018 p.1.) Real-life components, loading types and applications are often complex, and there are several situations, where variable amplitude loading can be found. Different industries that can be subjected to this loading type include automotive, railway and plant engineering. (Carpinteri et al. 2017, p. 1010.)

Application of different proof-loads such as over-pressure and over-speed have traditionally been conducted in mechanical components including cranes and pressure vessels and are included in some standards such as the ASTM international A391/A391M-07 (2012) for alloyed steel chains. Typically, no information on the influence on the structure's fatigue life or other properties is given. The purpose is, thus, assumed to be verification of integrity and quality of the structure. (Huther et al. 2022, p. 467; Fällgren et al. 2021, p. 948.)

The effect of overload on the fatigue life of a welded joint was studied by Huther et al. (2022). The applied overload improved the fatigue strength and caused a notable relaxation in residual stresses. The effect of the applied pre-load is based on factors including hardening and residual stresses. Another important cause is the plastic deformation on the material. (Huther et al. 2022, p. 467-476.)

For laser cut notches, variable amplitude loading and the effect of varying both high and low mean stress values was studied by Lipiäinen, Ahola & Björk (2022). In the study, a peak load was applied with following decreasing cycles. It was found that fatigue tests with high mean stress resulted in lower fatigue life when compared to results from constant amplitude loading. Furthermore, fatigue tests with low mean stress increased the fatigue strength significantly. The local performance was evaluated with a parametric fatigue assessment

approach, the 4R method. Further research could be conducted on welded joints to investigate the differences.

1.1 Objectives

The aim of this thesis is to study the effect of overload and variable amplitude (VA) loading on the fatigue strength of a welded joint and to examine the use of different analytical calculation methods to these cases. The effect of a tensile overload on the joint is studied also by measuring the residual stress levels of the joints before and after the overload. Two different levels of overload (OL1 and OL2) are applied before fatigue testing, and comparisons are made with the results from constant amplitude (CA) loading tests. Illustration of the applied loading types is presented in Figure 1.
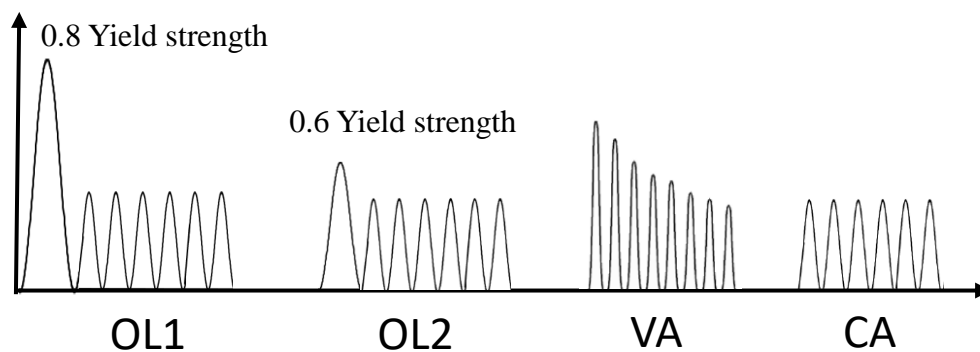
Figure 1. Illustration of the different loadings used in the thesis.

The fatigue strength is evaluated for a longitudinal non-load carrying (NLC) double gusset joint with three different steel grades. The examined joint type is presented in Figure 2. The steel grades under investigation are S355, S700 and S1100. The main material used in the thesis is steel grade S700, which is tested with all loading types extensively. Steel grades S355 and S1100 are acting as a control group for the overload cases to receive information on the changes in results brought by the yield strength. The OL1 with CA loading is performed on all materials.

Figure 2. Schematic drawing of the longitudinal double gusset.
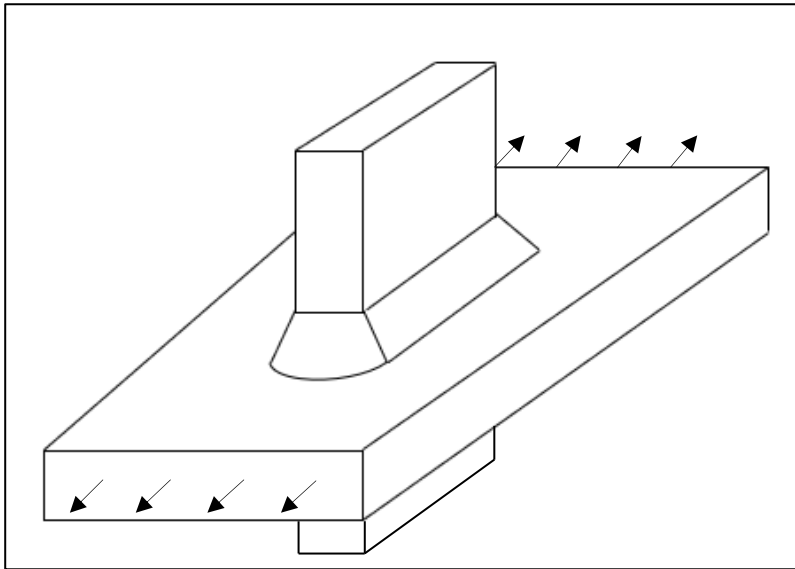
The study is conducted by using experimental and analytical methods. The analytical calculations are carried out by utilising different theories such as the 4R method, the theory of critical distances (TCD) and finite element method (FEM). The use of 4R as an analytical fatigue strength calculation method for variable amplitude loadings and overloads is also examined and evaluated. The focus of the thesis is, however, in reporting and analysing the experimental fatigue test results.

1.2 Research problem and questions

The research problem initiated from the lack of information on the effects of overload and VA loading to welds and their fatigue capacity. The main areas of interest include the fatigue lives of welded joints, the residual stresses before and after overload and the levels of local stress concentrations. As a limitation, the thesis does not take different joint types into consideration. The research questions can be stated as follows:

- What is the effect of overload and VA loading on the service life of the joint?

- How does applying overload affect the residual stress levels in the weld?

- How do the experimental test results correspond to the analytical calculations?

- Does the steel grade affect the possible phenomena?

1.3 Structure of the thesis

This thesis includes a literature review in Section 2, which aims to introduce the main terminology, theories and previous studies. The experimental research work is also described, and the analytical equations are presented in Section 3. In the results section, fatigue lives of the test specimens are documented with the analytical ones. Towards the end of the thesis in Sections 5 and 6, the results are analysed, and the reliability is evaluated.

2 Theory

This section consists of the key theories applied in the thesis and aims to present them and the terminology. The main theories included are the nominal stress method, effective notch stress (ENS), the TCD and the 4R method. Previous research on the effect of overloads and VA loading are also presented and described.

2.1 Fatigue phenomenon

Fatigue is a phenomenon in which structures crack under cyclic loading. These fatigue cracks start from locations that have high stress concentrations. In welds, the crack propagates typically from sharp transitions between the weld and its parent material. These locations include the weld toe and weld root. Figure 3 illustrates the possible failure locations in a welded joint. (Fricke 2013, p. 754-755.)
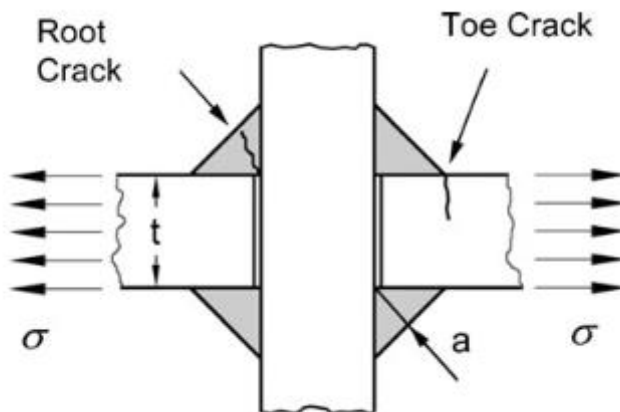
Figure 3. Example of failure locations in a welded cruciform joint (Fricke 2013, p. 754).

The fatigue resistance can be estimated with various methods that can be divided into three categories. These are methods that are based on pre-defined S-N curves and strains, methods based on the fatigue crack propagation analysis and the experimental methods that are carried out by testing structures. The most common calculation approaches based on the S-

N curves are nominal stress, structural hot spot stress and effective notch stress (ENS) methods. (Hobbacher 2016, p. 91.)

2.2 Nominal and structural stress approaches

The nominal stress method is a fatigue assessment approach in which estimations are made by using a characteristic S-N curve and a related FAT class. The FAT class can be further modified to take aspects such as post-weld treatments or wall thickness better into consideration. The approach is also based on the nominal stress which is the average global stress in the base plate as shown in tables of structural details or the weld throat. (Hobbacher 2016, p. 16 & 92-93.) The nominal stress range can be calculated as follows:

$$\Delta\sigma_{nom} = \sigma_{max} - \sigma_{min} \tag{1}$$

Where, $\Delta\sigma_{nom}$ is the nominal stress range, σ_{max} is the maximum stress and σ_{min} is the minimum stress. (Hobbacher 2016, p. 12.)

The fatigue resistance can be assessed in terms of cycles or stress (Hobbacher 2016 p. 92-93.) The fatigue life of a welded joint subjected to constant amplitude loading can be calculated with the following equation:

$$N_f = 2\cdot10^6 \cdot \left(\frac{FAT}{\Delta\sigma_{nom}}\right)^m \tag{2}$$

Where, N_f is the fatigue life, $\Delta\sigma_{nom}$ is the nominal stress range, m is the slope of the S-N curve and FAT is the design value for the stress range. (Hobbacher 2016, p. 92-93.)

2.3 Notch stress concepts

Notch stress concepts applied in the thesis are presented in this section. Theory and application to fatigue assessment are presented. The key theories presented are the ENS, TCD and 4R method.

2.3.1 Effective notch stress approach

The ENS is defined as the total fatigue-effective stress at the notch root acquired by applying a fictitious radius. It is calculated by assuming that the material has linear-elastic behaviour. In the ENS method, the actual weld toe shape is changed to a fictitious, effective one. This allows better consideration of non-linear behaviour and the alterations of weld shape. A notch radius of 1 mm can be used for the assessment of structural steels and aluminium alloys and has been confirmed to give coherent results. The fictitious radii are presented in Figure 4. The ENS method with the reference radius of 1 mm is applicable to evaluate different weld geometries but is limited to plate thicknesses of 5 mm or more. (Hobbacher 2016, p. 27-28.) When applied to welded thin sheets of below 5 mm, a reference radius of 0.05 mm or 0.3 mm can be applied. These options depend on both the plate thickness and location of failure. (Baumgartner, Hobbacher & Rennert 2020, p. 5-7.)
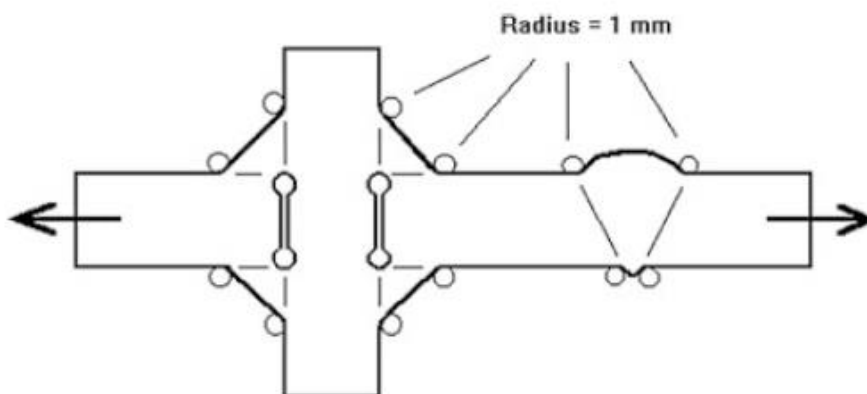

Figure 4. Effective radius applied to weld toes and roots (Hobbacher 2016, p. 27).

The ENS and can be obtained by various methods such as finite element models or parametric formulae. The finite element models can be created in a way that the tip of the effective radius is coincident to the root of the original notch. In the case of non-penetrating fillet welds, two shapes can be used. The possible shapes for the notch in the weld root include the keyhole and U-shape. The modelling can also be based on the actual, measured weld profile. In this case, idealization is usually implemented with straight and circular geometries. The recommended mesh quality and number of elements are presented in Figure 5 and Figure 6. (Hobbacher 2016, p. 28-29; Fricke 2010, p. 4-10.)
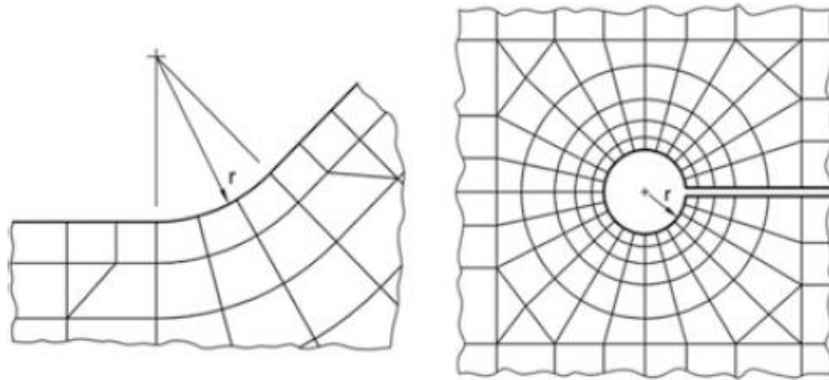
Figure 5. Recommendation on the mesh quality on the weld roots and toes (Hobbacher 2016, p. 29).

Element type	Relative size	Absolute size [mm]	No. of elements in 45° arc	No. of elements in 360° arc
Quadratic with mid-side nodes	≤r/4	≤0.25	≥3	≥24
Linear	≤r/6	≤0.15	≥5	≥40

Figure 6. Recommended number of elements on the curves (Hobbacher 2016, p. 29).

When the ENS is obtained with FE analysis, it is recommended that quadrilateral or hexahedral elements are used and that the minimum number of elements in a 45° arc is 3. For a 360° arc, the corresponding value is 24. (Baumgartner & Bruder 2013, p. 141;

Hobbacher 2016, p. 29.) The element sizes should not exceed 1/6 of the radius for linear elements and 1/4 for elements with higher order. The element sizes should be observed in both tangential and radial directions. (Hobbacher 2016, p. 29.)

2.3.2 Theory of critical distance

The TCD is a group of theories used to assess fatigue and failure. The methods included in the TCD are the point (PM), line (LN), area (AM) and volume (VM) methods. These methods have some similarities of which the most significant is the material related critical length L. Figure 7 presents the use of the TCD theories. (Taylor 2007, p. 21; González et al. 2019, p. 135.)

Line for the LM
(length 2L)

Area for the AM
(radius 1.32 L) or
Volume for the VM
(radius 1.54 L)
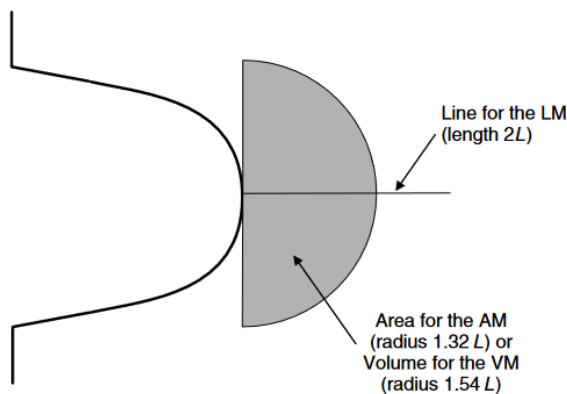
Figure 7. Application of the TCD methods to a notch (Mod. Taylor 2007, p. 29).

A stress analysis of the structure is required in the TCD method. The analysis should cover the area around the notches in precise. A linear-elastic analysis is utilised, and the analysis is usually carried out by FEM. In addition to the critical distance, the critical stress is also necessary to make the predictions. Figure 8 presents the stress levels of an analysed structure over a perpendicular distance. (Taylor 2007, p. 23.)
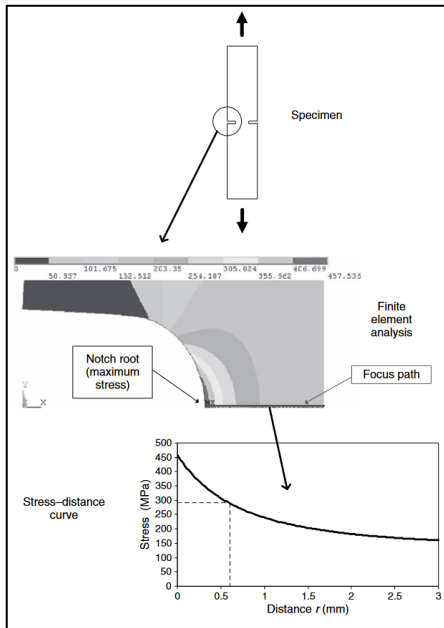
Figure 8. Stress levels along a perpendicular path through thickness (Taylor 2007, p. 22).

The most straightforward approach of the TCD theories is the point method. The PM method utilises the stress acquired $L/2$ from the notch root as a failure criterion. It is assumed that when the stress is below the critical one at the given number of cycles, σ_o, failure will not occur. (Taylor 2007, p. 24.) This assumption can be stated as follows:

$$\sigma_{\mathrm{eff}} = \sigma(L/2) \tag{3}$$

Where, $\sigma(L/2)$ is stress from distance $L/2$, L is the critical distance and σ_{eff} is the critical stress.

In the LN method, the stress-distance curve is obtained perpendicularly to the surface starting from the maximum stress concentration, and the stresses are used as average values. (Taylor 2007 p. 23-28.) Equation (4 describes the criterion of fracture according to the LN method. (Taylor 2007, p. 28; Baumgartner et al. 2015, p. 732).

$$\sigma_{eff} = \frac{1}{\rho} \int_0^\rho \sigma(x) \cdot dx \qquad (4)$$

Where, ρ is the microstructural length, $\sigma(x)$ is the stress course in the notch σ_{eff} is the effective stress.

The AM and VM methods of the theory are also based on averaged stresses. Instead of utilising a linear curve these methods depend on information on the stress levels on a specific area or volume near the notch. The average stress values can be obtained by post-processing the analysed FEM model. It should be considered that in these theories, the shape of the volume or area under examination has a significant impact on the results. These theories are also implemented less due to difficulty in application and less accuracy in predictions. (Taylor 2007, p. 29-30.)

2.3.3 4R method

The 4R method is a fatigue strength assessment approach for welded joints and cut edges, and it is based on the notch stress concept (Björk et al. 2018, p. 1286; Rohani Raftar et al. 2022, p. 2). The 4R method is used by conducting a mean stress correction in the linear-elastic range and by taking into account the elastic-plastic material properties at the root of the notch. The method also utilises the local stress ratio in the mean stress correction process. (Rohani Raftar et al. 2022, p. 2.) The necessary information on the joint and material are (Björk et al. 2018, p.1286):

- applied stress ratio, R

- residual stresses, $\sigma_{k,res}$

- geometrical quality of the weld toe, r_{true}

- ultimate strength of the material, R_m

This calculation method considers features such as the strength of the material, residual stresses, the weld quality, and the effective notch stress. The stress ratio is also applied. In the calculation of the maximum and minimum stresses, the Ramberg-Osgood (R-O) material

model and the kinematic hardening rule are utilised with Neuber's rule of hyperbolae and counter hyperbolae. (Rohani Raftar et al. 2022, p. 2; Ahola, Skriko & Björk 2019, p. 3-4.) The R-O material model is calculated by the following equations:

$$\varepsilon = \varepsilon_\varepsilon + \varepsilon_p = \frac{\sigma}{E} + (\frac{\sigma}{H})^{\frac{1}{n}} \tag{5}$$

$$\Delta\varepsilon = \Delta\varepsilon_e + \Delta\varepsilon_p = \frac{\Delta\sigma}{E} + 2(\frac{\Delta\sigma}{2H})^{\frac{1}{n}} \tag{6}$$

Where ε refers to the total strain, ε_p to plastic strain and ε_e to elastic strain. Stress is introduced as σ, E is the elastic modulus and H is the strain hardening coefficient. Symbol n refers to the strain hardening exponent. Symbols that have a Δ prior to them are the same variables as introduced before but refer to the ranges. (Ahola et al. 2019, p. 4.)

Equations 7 and 8 present the Neuber's rule with hyperbolae and counter hyperbolae. These equations are used with the R-O material model and kinematic hardening rule to acquire the maximum and minimum stresses. To solve the stresses, equations 5 and 7 are set to be of equal value as well as equations 6 and 8. (Ahola et al. 2019, p. 2-5.)

$$\varepsilon = \frac{\left(\frac{\Delta\sigma}{1-R} + \sigma_{k,\text{res}}\right)^2}{\sigma E} \tag{7}$$

$$\Delta\varepsilon = \frac{\Delta\sigma_k^2}{\Delta\sigma E} \tag{8}$$

In equation 7 and 8, R is the externally applied stress ratio, $\Delta\sigma_k$ is the notch stress range and $\sigma_{k,\text{res}}$ is the symbol for the local residual stress (Ahola et al. 2019, p. 2-5). The key value used in the 4R method is the local stress ratio (R_{local}) at the notch root. The local stress ratio is in

accordance with the local S-N curve. This behaviour is presented in Figure 9. (Rohani Raftar et al. 2022, p. 2.)
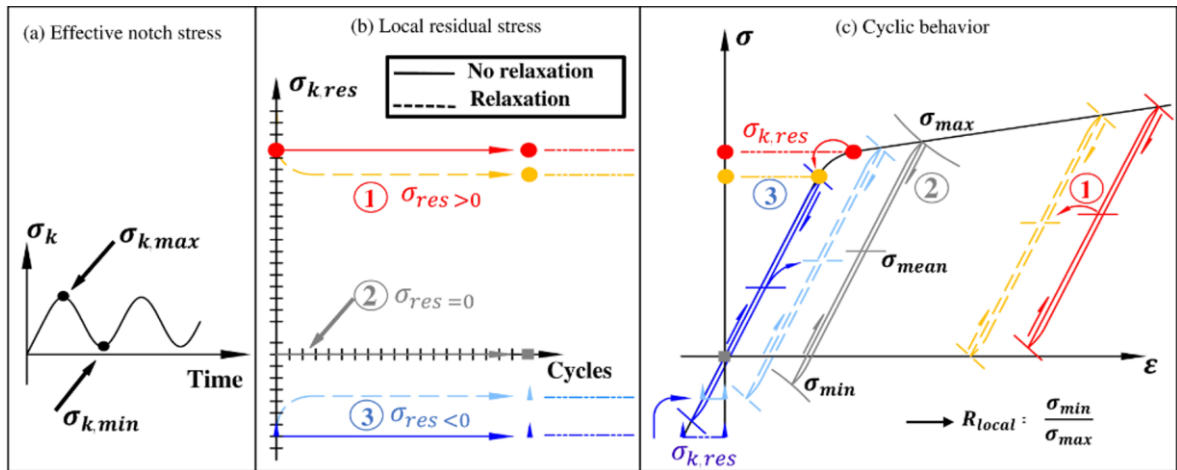
Figure 9. Illustration of the behaviour of welded joints that are subjected to constant amplitude loading (Rohani Raftar et al. 2022, p. 3).

The fatigue life of a welded joint is calculated using the 4R method with the following equation:

$$N_{f,4R} = (\frac{\sqrt{1 - R_{local}}}{\Delta\sigma_k})^{m_{4R}} C_{4R} \tag{9}$$

Where the $\Delta\sigma_k$ is the reference stress range, the m_{4R} is the S-N curve slope and the C_{4R} is fatigue capacity. (Ahola et al. 2019, p. 9.)

The application of the 4R method to variable amplitude loading has been studied and noted as applicable to assess the fatigue strength of welded joints in research by Nykänen et al (2017) and laser cut notches by Lipiäinen et al. (2022). The use of the 4R method is recommended in cases of variable amplitude loading as it has higher accuracy in complex cases than the traditional methods based on the fatigue class. It also has the ability to execute mean stress correction, which is valuable when assessing welds under variable amplitude loading. (Lipiäinen et al. 2022, p. 12-15.)

Essential remarks on the use of the method are that the 4R approach estimations of the damage sum are vastly similar to the damage sum results from experimental testing, and that the conservative predictions of damage sums are mostly less conservative than the experimentally derived ones. (Nykänen et al. 2017 p. 190.) The use of the TCD method is also applicable to the 4R method and proven valid when the damage parameter D is 1 (Lipiäinen et al. 2022, p. 13). In the calculation procedure for VA loads, the local stress ratio is determined for each cycle separately as well as the reference stress.

2.4 Previous research

Previous research has been conducted on the effect of overload on various themes. The topics cover the effect on the fatigue strength of welded joints, fatigue strength of metallic materials and crack propagation. This section introduces the studies relevant to the thesis.

2.4.1 Effect of overload on the fatigue strength

The effect of overload on the fatigue strength and behaviour of NLC joints was studied by Huther et al. (2022). In the study, experimental tests were conducted in tension ($R = 0.1$) on welded specimens with a longitudinal stiffener on both sides. The material of the joints was structural steel S355. Three overload levels were applied to the joints corresponding to the minimum yield strength (YS) value. The overload levels were 0.6 YS, 0.8 YS and 1 YS when considering the nominal stress value and yield strength of 355 MPa. Figure 10 presents the studied test specimen.
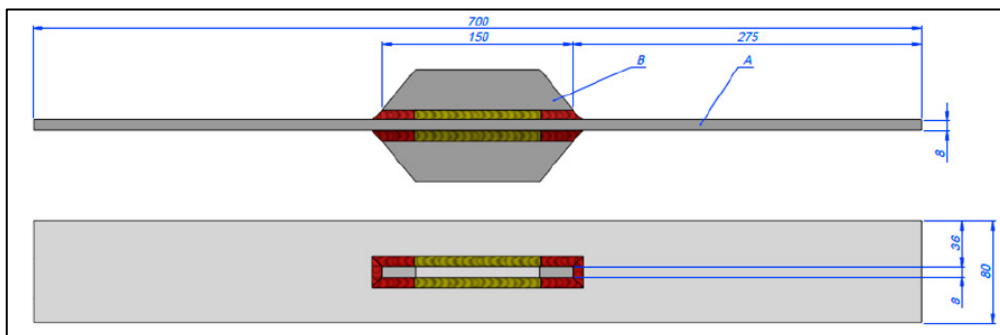

Figure 10. Investigated welded joint (Huther et al 2022, p. 468).

In the research by Huther et al. (2022), it was stated that the overload of 0.6 YS did not affect the fatigue strength. For overloads of 0.8 YS and 1 YS, the obtained fatigue values were 74 MPa and 99 MPa. An improvement by a factor of 1.57 was achieved with the 1 YS overload in comparison with the constant amplitude loading. Figure 11 presents the fatigue test results for overload cases of 0.8 and 1 YS. The results also showed a notable relaxation in residual stresses.
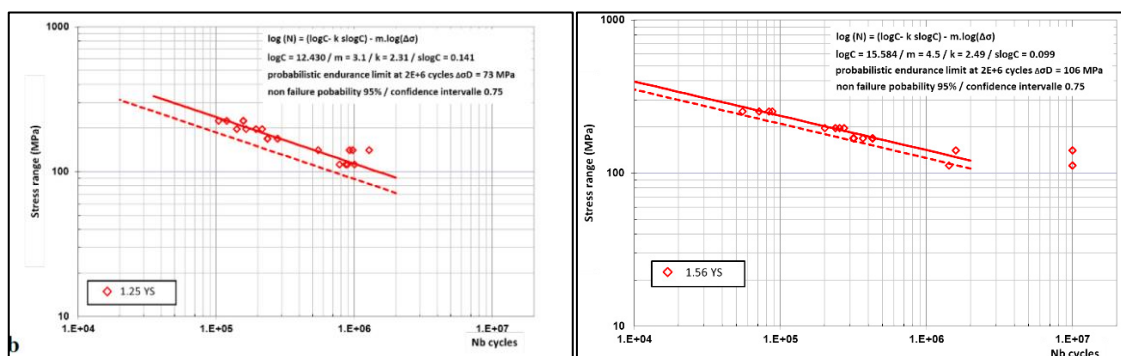
Figure 11. Fatigue test results for 0.8 YS and 1 YS overloads (1.25 YS and 1.56 YS corresponding to local stress) (Huther et al.2022 p. 474-475).

Hemmesi et al. (2022) investigated the effects of overload on the fatigue strength of metallic materials. This research did not cover welds. The tested specimens are presented in Figure 12. The net cross-section values were 12.56 mm^2 for specimen a) and 50.27 for specimen b). The materials under analysis were 42CrMoS4 steel and an aluminum alloy EN AW-6028. Two overload levels were used in the experiment. The overloads in the research were 75% (OL1) of the analytically estimated static strength and 75% (OL2) of the experimentally derived static strength. The analytically estimated static notch stress values were 1919 MPa for material 42CrMoS4 and 688 MPa for EN AW-6082. The experimentally derived ones were 3114 MPa and 1159 MPa, respectively. The nominal applied overloads with respect to notch stress values are presented in Table 1.
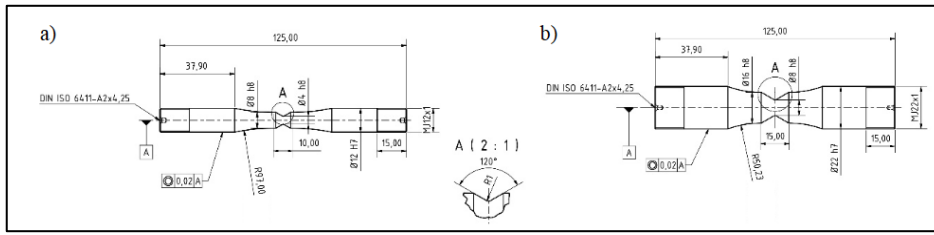
Figure 12. Investigated test specimens in the study by Hemmesi et al. (2022, p. 402).

Table 1. The applied nominal overload values with respect to notch stresses in the study by Hemmesi et al. (2022, p. 404).

Material	OL1 [MPa]	OL2 [MPa]
42CrMoS4	1440	2340
EN AW-6082	520	870

The fatigue test results by Hemmesi et al. (2022) are presented in Figure 13. The first overload level resulted in higher fatigue strength in comparison with the CA loading. A decrease of fatigue strength was, however, reported for the overload level 2 in respect to the first one. These results were explained by experimental observations on the overload cases that showed microscopic level plastic deformations. It should also be noted that in this study the stress ratio for the load was -1 and that the turn point for the overload was in compression.
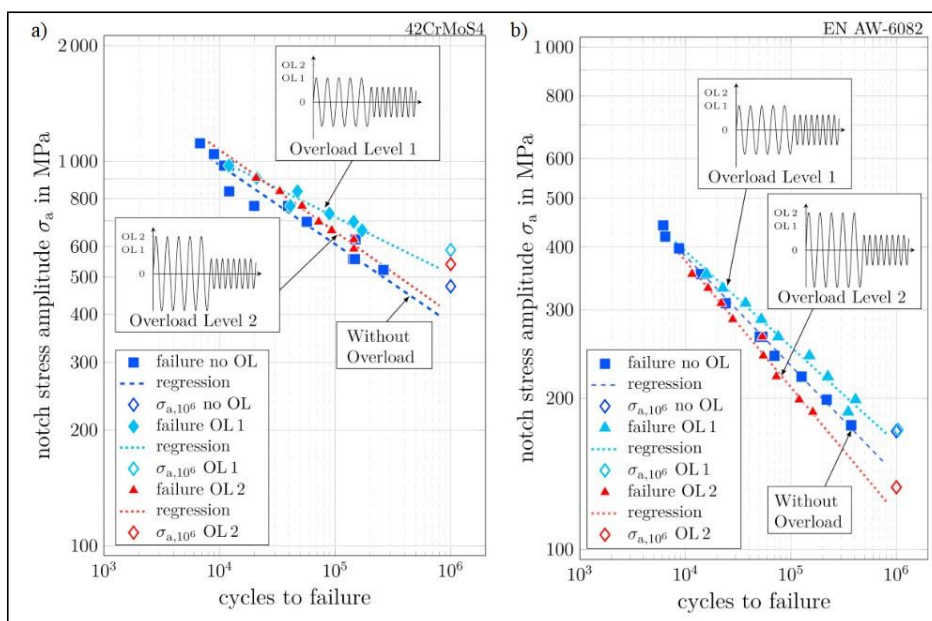
Figure 13. Fatigue strength results (Hemmesi et al. 2022, p. 405).

The possible improvement of fatigue limit by inducing tensile overload was studied by Mizukami et al. (2010). In the study, notched hot-rolled steel plates manufactured of material HT540 were tested. The test specimens were heat treated with 1000 ℃ air and quenched after. The geometry and measurements of the test specimens are presented in Figure 14. The testing was conducted by applying a single tensile overload of 1200 or 1000 MPa and a CA bending load. The stress ratio of the fatigue tests was 0.1. The loading pattern is presented in Figure 15. (Mizukami et al. 2010, p. 153-155.)
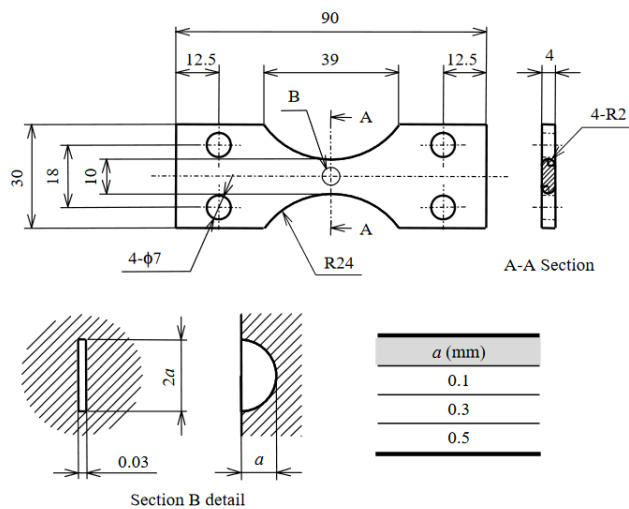
Figure 14. Geometry of test specimens (Mizukami et al. 2010, p. 155).
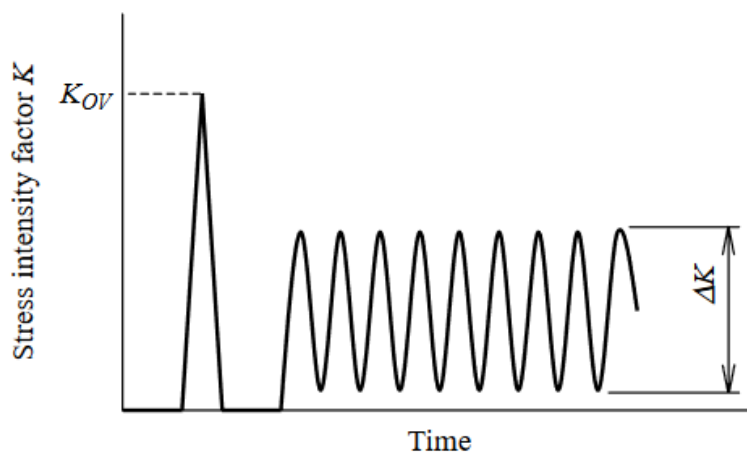
Figure 15. Applied loading and its pattern (Mizukami et al. 2010, p. 155).

The results showed that the threshold stress intensity factor was increased by the overload for test specimens with small notches. It was noted that the increase was dependent on the stress intensity factor of the overload. When the stress intensity factor for the overload was low, the amount of increase of the fatigue limit was similar for the larger notches. The improvement of the results was stated to be due to compressive residual stresses at the tip of the notch. It was, however, noted that overload beyond the yield strength did not have an effect. (Mizukami et al. 2010, p. 155-160.)

The studies by Huther et al. (2022) and Hemmesi et al. (2022) reported improvement in the fatigue strength of the examined specimen, when overload was applied. Similar results of improvement were also noted in a study by Mizukami et al. 2010 for hot-rolled steel HT540, Sahu et al. (2014) for 2024-T3 aluminum alloy and Lu, Yang & Chen (2019) for steel QSTE340TM. There were, however, results in which the overload had a neutral or negative effect on the fatigue strength of the material. The maximum achieved improvement on the fatigue strength of the longitudinal NLC joint was as high as 1.57 in comparison with the CA-loading (Huther et al. 2022 p. 475). The key aspects influencing the effect of the applied overload are noted to be relaxation of the residual stresses, local plasticity, and the level of overload. Lower overloads seem to have lower or even negative impact on the fatigue test results. (Hemmesi et al. 2022; Huther et al 2022; Mizukami et al. 2010; Lu et al. 2019.)

2.4.2 Effect of overload on the fatigue crack growth

Fatigue crack growth in structural steels experiencing underload and overload was studied by Liang et al. (2022). In this study, structural steels Q460C, S355J2W + N, Q550D, and Q690D were examined. The different loading conditions and spectra are presented in Figure 16 and Figure 17. The research compared CA loading, overload, underload, and periodic underloads.
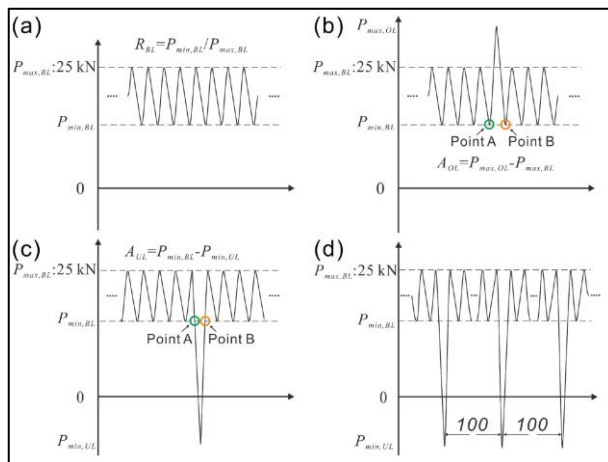
Figure 16. Applied loading conditions: (a) CA loading, (b) overload, (c) underload, and (d) periodic underloads (Liang et al. 2022, p. 5).

FCGR experiments under an OL on different structural steels.

Test condition	R_{BL}	$P_{max,BL}$ (kN)	$P_{min,BL}$ (kN)	$P_{max,OL}$ (kN)	A_{OL} (kN)
OL355–1	0.1	25	2.5	40	15
OL460–1					
OL550–1					
OL690–1					
OL355–2	0.5	25	12.5	40	15
OL460–2					
OL550–2					
OL690–2					

Figure 17. Experimental values for the research of fatigue crack growth (Liang et al. 2022, p. 5).

It was reported by Liang et al. (2022) that the single overload of 15 kN resulted in notable crack retardation, when the length of the crack was 18 mm. Furthermore, it could be noted that in the same steel grade the same overload with higher stress-ratio baseline resulted in even more obvious crack growth retardation. In different steel grades, the degree of crack retardation was reduced with the higher strength materials. The effect of overload on the fatigue crack growth is presented in Figure 18.
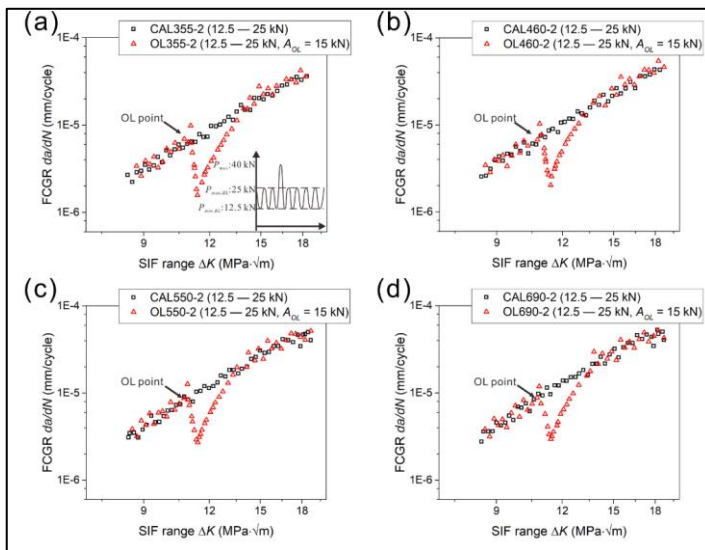
Figure 18. Effect of overload on the fatigue crack growth of different materials: (a) S355, (b) Q460C, (c) Q550D and (d) Q960D (Liang et al. 2022, p. 9).

The effect of overload on the crack propagation for high-strength steels was studied by Simunek et al. (2018). The investigated materials were steel grades S960 and S355. The geometry and measurements of the notched test specimen is presented in Figure 19. The test specimens had a single 5 mm deep notch to initiate the crack growth. The crack lengths were measured using optical systems and indirect potential drop method.
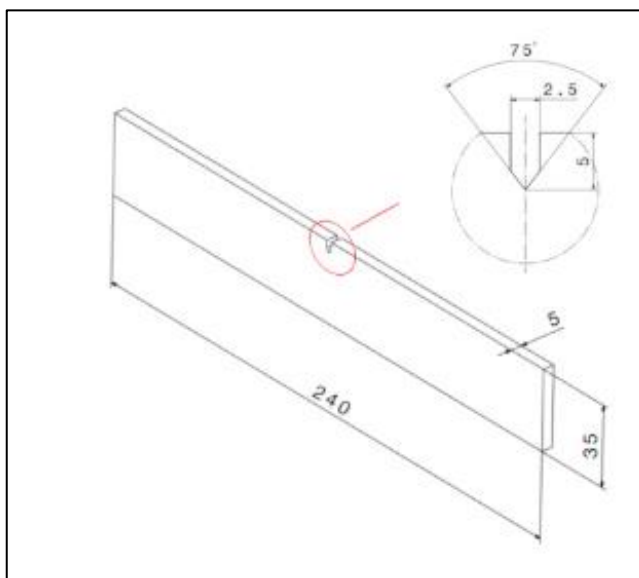
Figure 19. Investigated test specimen (Simunek et al. 2018, p. 338).

The fatigue tests were conducted with 0.1 stress ratio. Both CA load and CA load with single overload were performed. The overload was applied during testing at the crack length of 8.5 mm. The nominal stress range for steel grade S355 was 62.5 MPa and the overload was calculated from the CA stress range with a ratio of 2. For overload cases and steel grade S960, a higher stress range of 122.25 MPa was applied with overload calculated with a ratio of 2. (Simunek et al. 2018, p. 335-345.)

The overload resulted in a significant retardation of the crack growth and extended the service life for both steel grades. It was stated that the overload resulted in 1.14 times longer crack growth period for S960 and 1.41 for S355. The crack growth rates and retardations after the tensile overload can be seen in Figure 20 and Figure 21. (Simunek et al 2018, p. 341-344.)
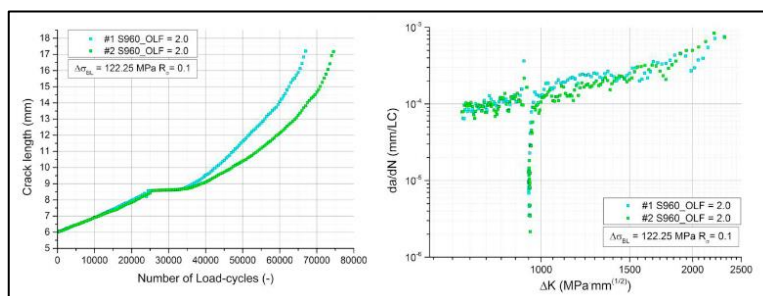
Figure 20. Crack growth rates and retardation for steel grade S960 with tensile overload (Simunek et al. 2018, p. 341).
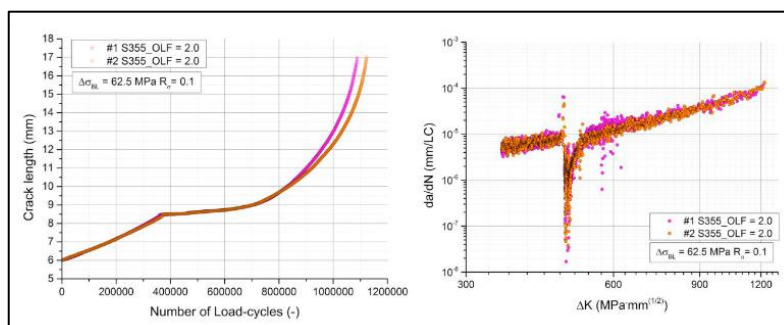
Figure 21. Crack growth rates and retardation for steel grade S355 after tensile overload (Simunek et al. 2018, p. 341).

3 Methods

This section presents the methods utilized in the thesis. The focus is on reporting the initial values applied in the experimental research and describing the analytical calculations. Furthermore, the experimental settings and test types are described. The main method applied in the thesis is the experimental fatigue testing of the welded joints under overload, CA and VA loading. The fatigue test results are then evaluated with different methods such as the 4R, the ENS and the TCD method.

For fatigue analysis, FE analysis is conducted, and the FE models are presented. The geometry, element type and materials are given as well as the loads, constraints and the analysis type. The mesh sizes are presented with information on the applied fictitious radius. The FE models are created based both the ideal and real geometries of the specimen. This allows better understanding of the fatigue strength and the factors affecting it.

3.1 Materials

The test specimens were manufactured of three different materials with corresponding filler materials. The main material in the experiments was SSAB Strenx 700 MC Plus and the materials acting as a control group were SSAB Domex 355 MC and SSAB Strenx 1100 MC Plus. The mechanical properties and chemical compositions of the steel grades are presented in Table 2 and 3, respectively.

Table 2. The nominal mechanical properties of SSAB Domex (355 MC) and Strenx steel grades (SSAB 2023a-c).

Material	t	$R_{p,0.2}$	R_m	A_5
	[mm]	[MPa]	[Mpa]	[%]
355 MC	8	355	430–550	23

Table 2 continues. The nominal mechanical properties of SSAB Domex (355 MC) and Strenx steel grades (SSAB 2023a-c).

Material	t	$R_{p,0.2}$	R_m	A_5
	[mm]	[MPa]	[MPa]	[%]
700 MC Plus	8	700	750–950	13
1100 MC Plus	8	1100	1250–1450	7

Table 3. The nominal chemical compositions of SSAB Domex (355 MC) and Strenx steel grades (SSAB 2023a-c).

Material	Contents in the material [weight - %]								
	C	Si	Mn	P	S	Al	Nb	V	Ti
355 MC	0.056	0.02	0.92	0.013	0.005	0.047	0.027	0.009	0.001
700 MC Plus	0.056	0.18	1.81	0.01	0.003	0.035	0.081	0.014	0.108
1100 MC Plus	0.129	0.18	1.48	0.006	0.002	0.048	-	-	-

The matching filler material used for the steel grade S355 was OK Autrod 12.51 by ESAB. The welding consumable is coated with copper and can be used for the common structural and engineering steels. For the steel grade S700, the filler material was OK 69.25 by ESAB. OK 69.25 filler material is a coated stainless electrode, which results in austenitic Cr-Ni-Mo weld material. The weld material has an increased N and Mn content. (ESAB 2023a-b).

Union X 96 filler material was used for welding the S1100 steel grade. Union X 96 filler material has good deformability and can be used for heat treated steels and thermomechanically rolled structural steel in different applications such as construction of

cranes. (Voestalpine 2023). Table 4 and Table 5 present the mechanical properties and chemical compositions for all the filler materials used in welding.

Table 4. The mechanical properties of the filler materials (ESAB 2023a-b; Voestalpine 2023).

Filler material	$R_{p,0.2}$	R_m	A_5	Impact strength
	[MPa]	[MPa]	[%]	[J / 20°C]
OK 12.51 ESAB	460	560	26	130
OK 69.25 ESAB	450	650	35	90
Union X96 Böhler	930	980	14	80

Table 5. The typical chemical compositions of the filler materials (ESAB 2023a-b; Voestalpine 2023).

Filler material	Contents in the material [weight - %]					
	C	Mn	Si	S	Ni	Mo
OK 12.51 ESAB	0.10	1.11	0.72	0.012	-	-
OK 69.25 ESAB	0.04	6.5	0.5	-	16	3.0
Union X96 Böhler	0.12	1.90	0.82	-	2.35	0.55

3.2 Specimen geometry

The experiments were conducted on a longitudinal NLC joint with gussets on both sides. All plates, including the gussets, have the thickness of $t = 8$ mm. The applied shape and main

dimensions of the welded joint are presented in Figure 22 and Figure 23, and a more detailed manufacturing drawing of the applied gusset in Figure 24. The main area of interest in the experiments and analysis was the narrower section of the joint where the base plate is 80 mm wide. The longer geometry in Figure 23 was used only with steel grade S700 and VA loading due to constraints set by the fatigue test machine.
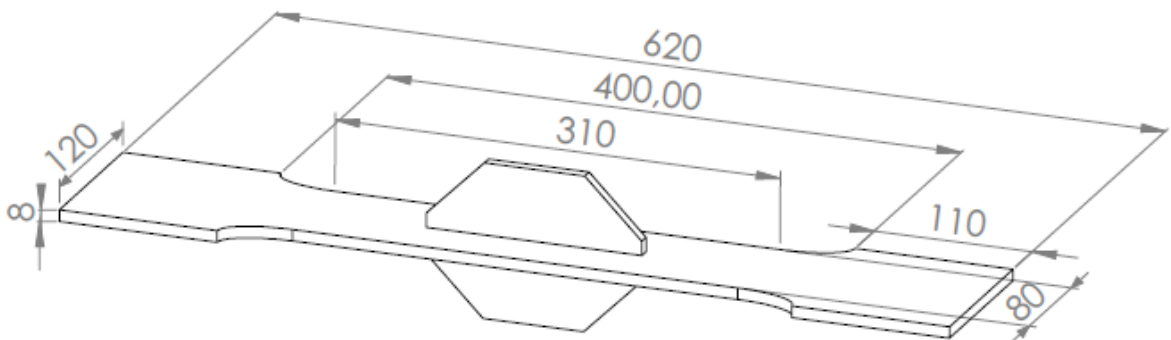
Figure 22. Main shape and dimensions (in mm) of the welded joint for steel grades S355, S700 and S1100.
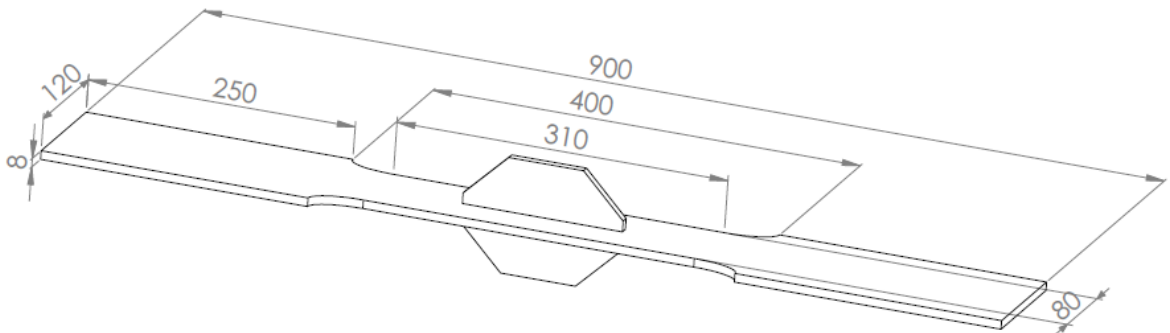
Figure 23. Main shape and dimensions (in mm) of the welded joint for steel grade S700 and VA loading.
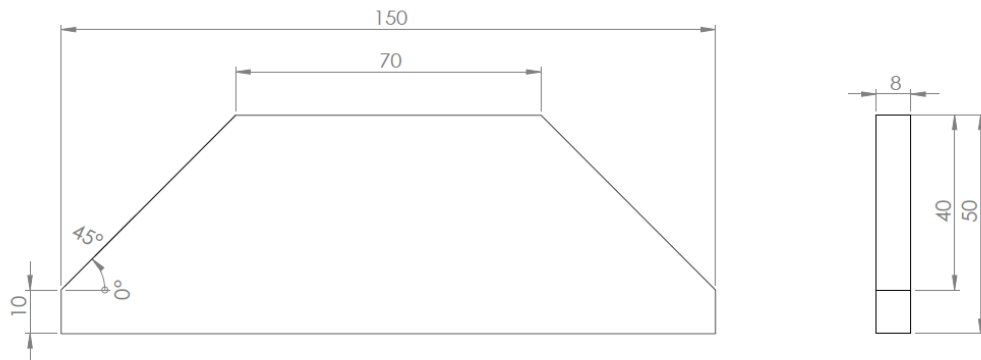
Figure 24. Shape and dimensions (in mm) of the gusset applied to all steel grades.

The shape presented in Figure 22 was applied to cases with over and CA loading and was used with steel grades S355, S700 and S1100. The gussets were manufactured accordingly to have similar material with the base plate. The material values provided by the material certificates and used in calculations are presented in Section 3.6.

3.3 Manufacturing

The joints were manufactured out of sheet metals by laser cutting and welding. The surface of the cut steel was cleaned after laser cutting with 10 % citric acid to improve the quality of welding. Three tack welds were placed on both sides of the gusset on equal distances of approximately 30 mm. Figure 25 presents a tack welded joint. As only one weld toe was examined in the fatigue tests, the others were post-processed with HFMI (high frequency impact treatment). The post-processing was also to ensure that the crack propagation would begin at the designated weld toe.

Figure 25. Investigated joint with tack welds.

3.3.1 Welding

The joints were welded with GMAW (gas metal arc welding) process, and the welding was carried out by using a robotised system. The robotised system was chosen to achieve consistent quality of the welds. No grooves were machined to the joints. The welding set-up and clamping of the specimen can be seen in Figure 26. The gussets were welded around with two passes on each side of the base plate with a target throat thickness of 4 mm. The start and end points of the weld passes were located middle in longitudinal direction of gusset. The welding sequence is presented in Figure 27. The full welding procedure specifications for each material are shown in Appendix I.

Figure 26. Welding set-up and clamping of specimen.
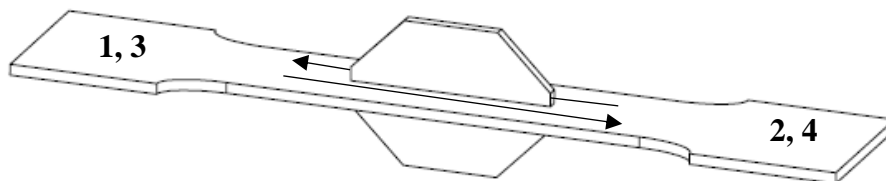
Figure 27. Welding sequence of the double gusset joint.

The shielding gas used with all steel grades was Argon with 8 % CO_2. The shielding gas had a flow rate of 14 l/min. Average welding parameters are presented in Table 6 and full list of parameters is presented in Appendix II. In the welding process, the filler material's contact tip to work distance was 18 mm. The torch and inclination angles were also of constant value with the torch angle being 45° and the travel angle 5° pushing.

Table 6. Average welding parameters for all welds and passes.

Steel grade	U [V]	I [A]	v_{wire}* [m/min]	v* [mm/s]	T_0* [°C]	Q [kJ/mm]	$t_{8/5,2D}$ [s]	$t_{8/5,3D}$ [s]
S700	26.0–27.0	213–228	11	7.8	20	0.57–0.61	3.9–4.4	2.0–2.2
S355	26.8–27.1	223–228	11	7.8	20	0.63–0.62	4.5–4.7	2.2
S1100	25.5–25.9	220–225	11	7.8	20	0.58–0.63	4.0–4.2	2.1

*Constant values

The heat input can be considered as one of the key factors in the properties of ferritic and ferritic-austenitic steel welds and should be considered for different welding processes. The cooling rate also has a crucial effect on the weld quality as too abrupt cooling may lead to hardening, softening or cracking of the material. (EN 1011-1 2009, p. 10-12; EN 1011-2 2001, p. 41) The heat input and cooling rates were calculated for each weld run with the following equations:

$$Q = k \cdot \frac{U \cdot I}{v} \cdot 10^{-3} \tag{10}$$

$$t_{8/5} = (4300 - 4.3T_o) \cdot 10^5 \cdot \frac{Q^2}{t^2} \cdot \left[\left(\frac{1}{500 - T_0} \right)^2 - \left(\frac{1}{800 - T_0} \right)^2 \right] \cdot F_2 \tag{11}$$

Where, Q is the heat input, U is the voltage, k is the thermal efficiency, I is the welding current and v is the travel speed. In equation 11, $t_{8/5}$ is the cooling rate, T_0 is the interpass temperature, t is plate thickness and F_2 is the shape factor. (EN 1011-1 2009, p. 10-12; EN 1011-2 2001, p. 41)

3.3.2 Post-weld treatments

Only one weld toe was selected from each test specimen to be examined. The weld toe was selected on the basis of angular distortion to be on the concave side of the base plate. Weld quality was also examined and the weld with highest quality was chosen. The other three weld toes were post-processed by utilising HFMI. As HFMI treatment improves the fatigue strength of a material, it can be estimated that the weld toe in as-welded condition will experience fatigue failure first and, furthermore, the strain gauge can be positioned to the specific weld toe (Weich et al. 2009, p. 322-324). Figure 28 presents the weld toes after post-processing.

Figure 28. HFMI post-processed weld toes and equipment.

3.4 Description of fatigue tests

The fatigue tests were executed with three different loading types to verify the analytical calculations. The applied loading types were CA, VA and CA loading pre-loaded with an individual tension overload. All steel grades were tested with OL1 and CA loading. The number of tested joints for each loading type and material are presented in Table 7. All fatigue tests were carried out under tension. The applied stress ratio R was 0.1 for all tests except the cases with VA which had a stress ratio of 0.05.

Table 7. Number of fatigue tests conducted for each material and loading type.

	Load type			
Material	CA	OL1 & CA	OL2 & CA	VA
S700	6	7	6	2
S355	2	6	-	-
S1100	2	6	-	-

The overloads were set on two levels and applied to the structures statically. The first overload (OL1) corresponds to 0.8YS and the second (OL2) to 0.6YS considering the nominal stress level. The yield strength values were assumed to be the minimum values that were provided by the manufacturer and presented in

Table 3. The maximum overload level was set to be near the yield strength of the material to receive results of an extreme case. The lower level was considered to be below the highest, but still enough to notice a plausible difference in results. It is also close to the static design limit for a welded structure. The complete test matrixes for each material containing the specimen ID numbers and fatigue test results can be found in Appendix III.

3.4.1 Experimental set-up

The fatigue tests were conducted at LUT university in the laboratory of steel structures. All tests except the cases with VA loading were performed by utilising high-capacity full resonance machine. The experimental set-ups are presented in Figure 30. The fatigue tests with VA loading were conducted on a servo-hydraulic test rig (400 kN capacity). Fatigue tests were executed in tension with the applied stress ratio of 0.05 for VA cases and 0.1 for others. Stress ratio of below 0.5 has been recommended by Hobbacher (2016 p. 63).

The experimental analysis of the fatigue strength was based on information gathered with electric resistance strain gages. The strain gages were applied to the weld toes according to IIW (International Institute of Welding) recommendations and thus the location of the single

strain gage was determined to be 0.4*t* from the weld toe. This distance equals 3.2 mm for an 8 mm thick plate. A single strain gage has been found adequate in research and can, thus, be applied in the thesis. For more precise results, two strain gages should, however, be considered. The strain gage grid size limit in the experiments was 0.2*t* and the applied size was 1.5 mm. (Hobbacher 2016, p. 17-25; Niemi, Fricke & Maddox 2006, p. 11-12) Figure 29 presents the test specimen with the inserted hot spot strain gage and its location.
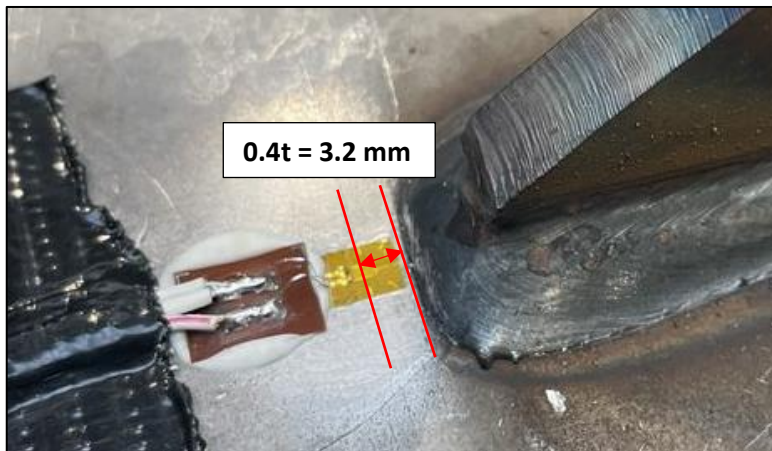
Figure 29. Applied strain gage and its position.
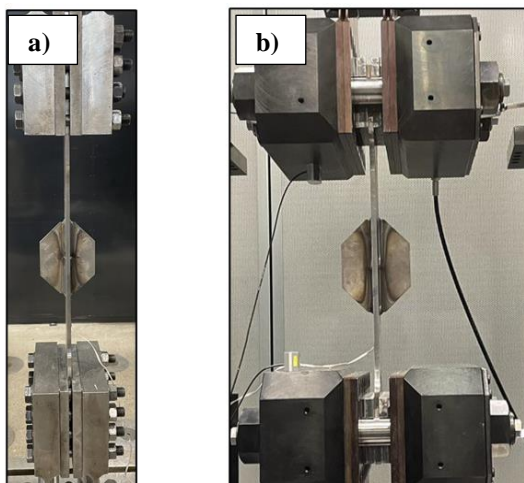
Figure 30. The fatigue test rigs and setups a) Servo hydraulic rig (400 kN) b) High-capacity resonance rig. The clamping distances were 487 mm for a) and 400 mm for b).

The strain gages were utilised to measure the hot-spot (HS) stress in the test specimens and to evaluate the levels of membrane and bending stress components. The stress was

determined with the measured strain values and material properties. The following equation was used in the calculation:

$$\sigma_{HS} = E \cdot \varepsilon_{SG} \qquad (12)$$

Where, σ_{HS} is the hot-spot stress, E is the elastic modulus and ε_{SG} is the strain value. (Niemi et al. 2006, p. 13)

3.4.2 Supportive tests

Supportive tests were conducted to gain information on the effects of overload on the welded joint. The tests included residual stress measurements, 3D-scanning and examining the polished cross-sections. The polished cross-sections were manufactured from the centre line of the joint in two directions to cover both the continuous welds and the weld toe area. One specimen of each test series was measured.

The residual stresses were measured with an X-ray diffractometer. The used machinery was XSTRESS 3000 with G3-goniometer by Stresstech. The stresses were measured before and after applying the overload to define the potential differences and relaxation. In the residual stress measurements, the number of tilts was three and the tilt angles were -30º/30º with +1º oscillation. The used collimator had the diameter of 1 mm. The stresses were measured along the centre line of the specimen. Figure 31 presents the residual stress measurements and set-up. Residual stresses were measured before and after the static tensile overload. Additional tests were made also on the effects of the HFMI treatment on the welded joint.
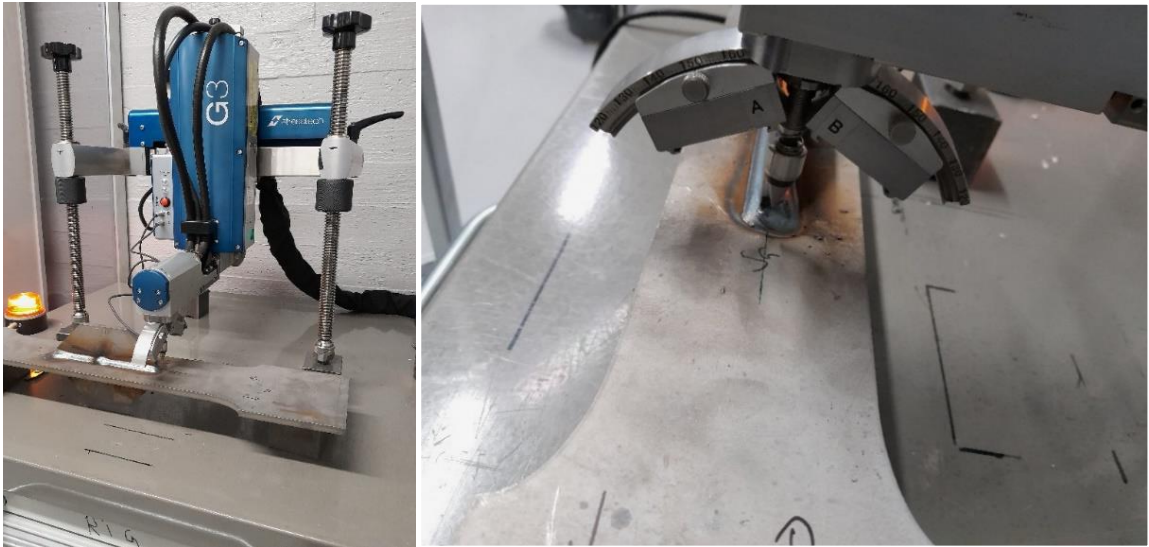
Figure 31. Residual stress measurements set-up and machinery.

The geometries of the welded joints were defined with a 3D-surface scanner HP-L-20.8 with ROMER Absolute Arm. The overall profiles were scanned to define the overall geometries and angular distortions. The examined weld toe was scanned with higher resolution. One specimen was scanned with a profilometer to receive more precise images of the weld toe and its radius.

3.5 Finite element analysis and the used element model

The FE analysis was conducted by utilising FEMAP/NX Nastran software. The double gusset joint was modelled with solid elements and two different notch approaches. The element models were created with 1 mm and 0.05 mm radii according to the ENS and TCD methods. Symmetry of the joint was utilised and only 1/8 of the geometry was modelled. An example of the FE model and its geometry applied in the thesis is presented in Figure 32.
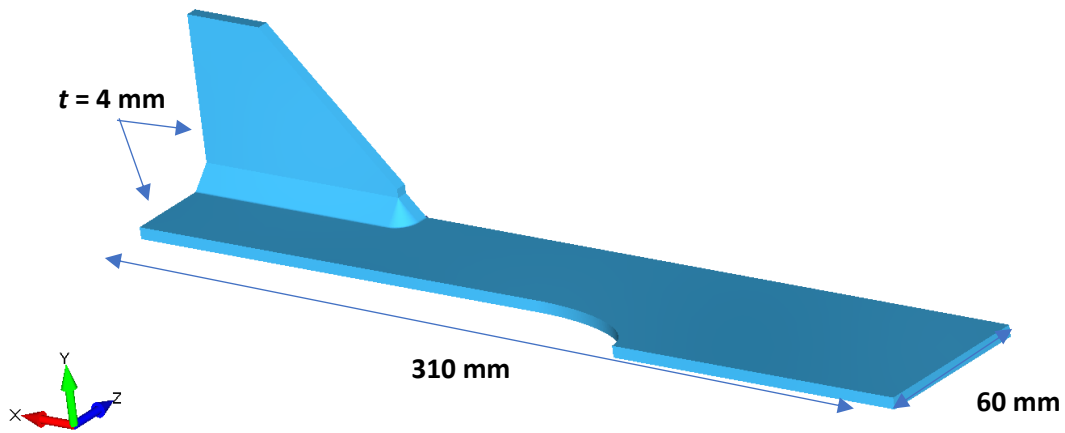
Figure 32. Symmetry model and main measurements of the welded joint.

The geometries of the actual test specimens were modelled based on the information received from 3D scanning and other measurements. In these models, the angular distortion was taken into consideration as well as the actual notch radius. The bending stress component due to angular distortion was analysed by defining a bending load in the ENS model. The geometries were modelled with ENS and TCD methods for comparison.

3.5.1 The geometry, element type and material

Two different notch radiuses were applied in the models. The ENS models have a weld toe radius of 1 mm or true radius that was additioned to the 1 mm one. The TCD models have a 0.05 mm notch radius. The typical meshes applied to the areas near the notch are presented in Figures 33 and 34. The angular distortion was considered with a bending load case. In these models, 1/4 of the joint was modelled to simulate the constraints correctly.
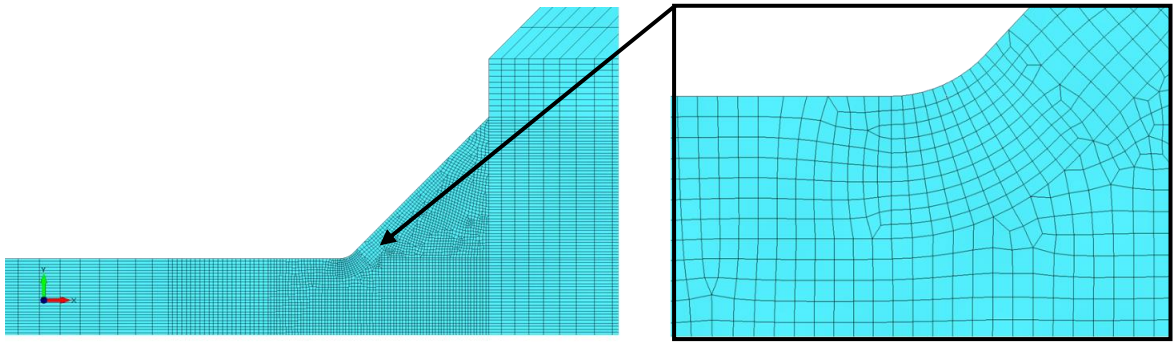
Figure 33. A typical mesh applied to the ENS model with 1 mm notch radius.
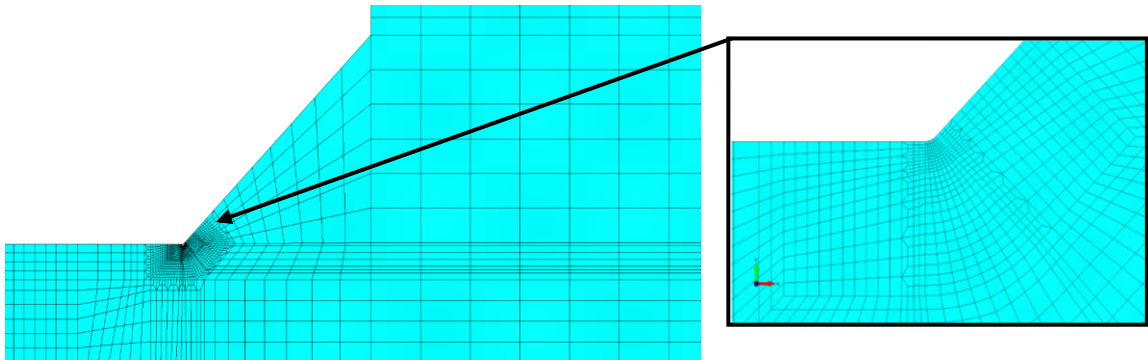
Figure 34. A typical mesh applied to the TCD model with 0.05 mm notch radius.

The number of elements used in the 45° arc was 10-12 for the ENS models and 8 for the TCD models. In the TCD models, the element size near the notch radius was 0.01 mm along a 0.1 mm distance. The material values for all models were, elastic modulus E = 210 000 MPa and Poisson's ratio v = 0.3. The material model was linear elastic.

3.5.2 Loads, constraints and, analysis

The nominal load of 1 MPa was applied to all FE models to obtain the stress concentration factor for membrane stress. The corresponding values were used for bending load for calculation of the stress concentration factor for bending. The loading was applied as force per area and calculated to match the stress on the narrower section of the specimen. As the geometry was modelled utilising symmetry, the constraints were set accordingly, and

symmetry constraints were applied. Figure 35 presents the applied load and constraints for the models with nominal load. The analysis type was linear-static in all analysed cases and loading was applied as force per area on the surface.
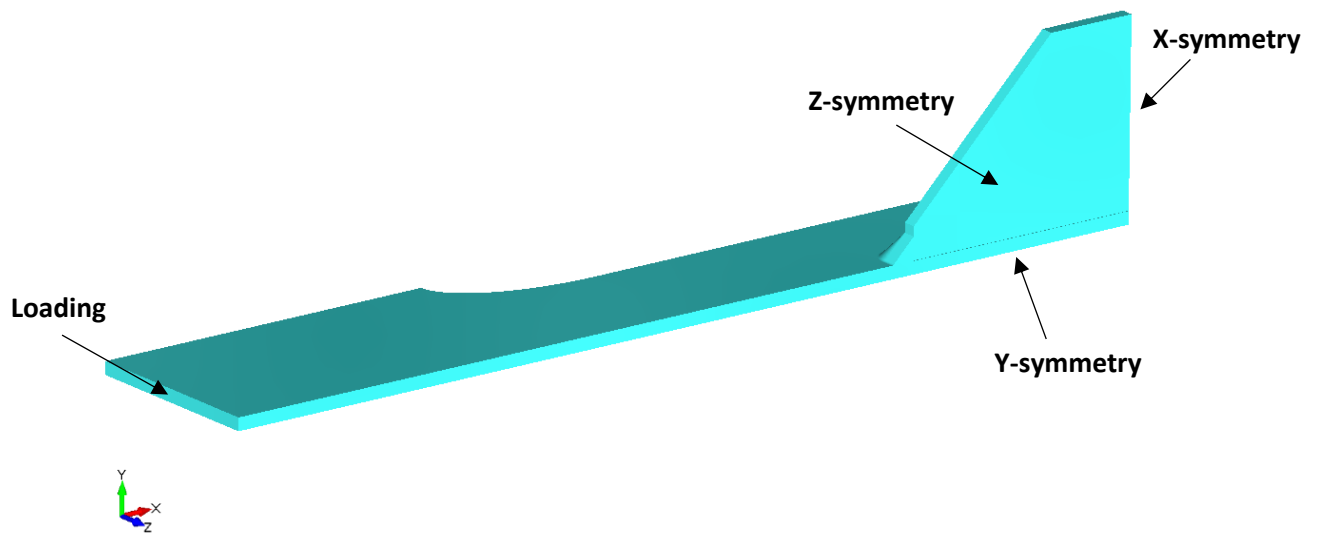
Figure 35. Loads and constraints applied to the models with membrane load.

3.6 Application of the 4R method to the overload and variable amplitude cases

Analytical calculations were made to evaluate the fatigue lives of the joints and to validate the calculation methods. The 4R method was applied to the overload cases by defining the local stress values caused by the fatigue loading. Figure 36 illustrates the stress and strain behaviour of the welded joint in the constant amplitude and overload cases. The numbered locations aim to depict the different stages of the applied loading.
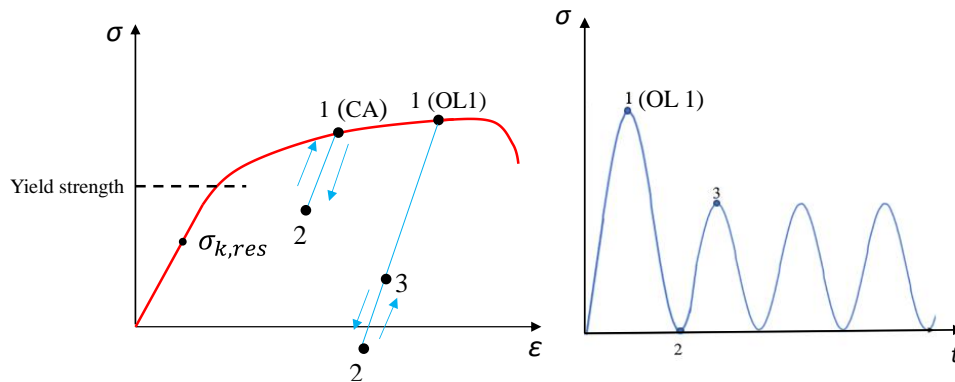
Figure 36. Schematic drawing of the local behaviour of the welded joint under CA and OL + CA loading types.

The overload causes a high local stress in the structure that is presented in Figure 36 with label 1 for the first overload level. The maximum local stress was obtained by applying the R-O material model (equation 5) and Neuber's rule with hyperbolae (equation 7) in the following manner:

$$f(\sigma_{max}) = \frac{\sigma_{max,loc}}{E} + \left(\frac{\sigma_{max,loc}}{H}\right)^{\frac{1}{n}} - \frac{(\sigma_{k,res} + \sigma_k)^2}{\sigma_{max,loc} \cdot E} = 0 \tag{13}$$

Where, $\sigma_{max,loc}$ refers to the maximum local stress, E is the elastic modulus, H is the strain hardening coefficient, n is the strain hardening exponent, $\sigma_{k,res}$ is the residual stress and σ_k is the maximum applied nominal stress.

After the overload, the difference from maximum to minimum stress level is calculated with Neuber's rule of counter hyperbolae and R-O material model. This difference can be seen in Figure 36 between locations one and two. The minimum stress could be obtained by subtracting the stress difference from the maximum stress. The stress difference and minimum stress were calculated as follows:

$$f(\Delta\sigma) = \frac{\Delta\sigma}{E} + 2 \cdot \left(\frac{\Delta\sigma}{2H}\right)^{\frac{1}{n}} - \frac{\Delta\sigma_k^2}{\Delta\sigma \cdot E} = 0 \tag{14}$$

$$\sigma_{\min,\text{loc}} = \sigma_{\max,\text{loc}} - \Delta\sigma \tag{15}$$

Where, $\sigma_{\min,\text{loc}}$ refers to the minimum local stress, $\Delta\sigma$ refers to the local stress difference, $\Delta\sigma_k$ is the nominal stress range.

The difference from the minimum stress to the peak of the constant amplitude loading was calculated by applying equation 14 again and adding the difference to the minimum stress value. This difference between the minimum stress and the stress caused by the peak of the CA loading defines the new mean stress level for the cyclic fatigue loading. Theoretically, the overload would lead to lower mean stress values in comparison with the CA loading. This phenomenon can also be seen in Figure 36.

Two different material parameters were tested in the calculation process of the 4R method to evaluate its effect. Strain hardening coefficient and strain hardening exponent were varied. The elastic modulus was assumed to be 210 GPa. The different material values tested in the thesis are presented in Table 8. The material values of the second row were derived from a research article by Amraei et al. (2019).

Table 8. Material parameters applied in the calculation process of the 4R method.

E	H	n
[MPa]	[MPa]	[-]
210 000	1.65 R_m	0.15
210 000	1000	0.052
	R_m	
	[MPa]	
S700	S355	S1100
821	481	1153

For variable amplitude cases, a block type loading was applied with a stress ratio of 0.05. The VA loading was designed to have a high peak load at the beginning and following descending cycles. Overall, the loading included 10 000 cycles. Information on the loading is presented in Table 9. The nominal stress ranges for the blocks were calculated as a load spectrum utilizing the information provided in a study by Köhler et al. (2017) in the following manner:

$$H_i = H_0 \exp\left\{-\ln H_0 \left(\frac{\Delta\sigma_{\mathrm{nom},i}}{\Delta\sigma_{\mathrm{nom,max}}}\right)^{\nu_G}\right\} \tag{16}$$

$$\Delta\sigma_{\mathrm{nom},i,p} = \left\{\frac{\Delta\sigma_{\mathrm{nom},i}}{\Delta\sigma_{\mathrm{nom,max}}}(1-p)+p\right\}\Delta\sigma_{\mathrm{nom},i} \tag{17}$$

Where, $\Delta\sigma_{\mathrm{nom},i}$ is the nominal stress range, $\Delta\sigma_{\mathrm{nom,max}}$ is the nominal maximum stress range, H_0 stands for the number of cycles in a block, ν_G is the Gaussian shape factor and p is the scaling factor. (Lipiäinen et al. 2022, p. 6-7.) Values 0.3-0.4 and 2 were applied as scaling factors and Gaussian shape factor, respectively.

Table 9. Information on the stress levels and load spectrums of the VA loading.

	$\Delta\sigma_{\mathrm{nom,max}}$ [MPa]	$\Delta\sigma_{\mathrm{nom,min}}$ [MPa]	$\Delta\sigma_{\mathrm{eq}}$ [MPa]
Load spectrum 1	525	158	245
Load spectrum 2	540	162	252
Load spectrum 3	540	232	300
Load spectrum 4	475	143	221

The principle of the loading is presented in Figures 1 and 37. The 4R method was applied by utilizing Palmgren-Miner rule for linear damage and the ENS method intended for CA cases. FAT class of 225 MPa was used in the calculation. The local stress levels and ratios were analyzed for each cycle separately and the fatigue lives of the joints were estimated with the equivalent stress concept. Furthermore, the Smith-Watson-Topper (SWT) rule for mean stress correction was applied and the equivalent stress range was calculated with the following equation:

$$\Delta\sigma_{k,\text{eq}} = \sqrt[m]{\frac{1}{D} \frac{\sum_i n_i \left(\dfrac{\Delta\sigma_{k,i}}{\sqrt{1-R_{\text{local},i}}}\right)^m}{\sum_i n_i}} \tag{18}$$

Where, $\Delta\sigma_{k,\text{eq}}$ is the equivalent stress range, D is the damage parameter, n is the amount of cycles for a block, $R_{\text{local},i}$ is the local stress ratio for a block and m is the slope of the curve. (Lipiäinen et al. 2022, p. 3-4.)
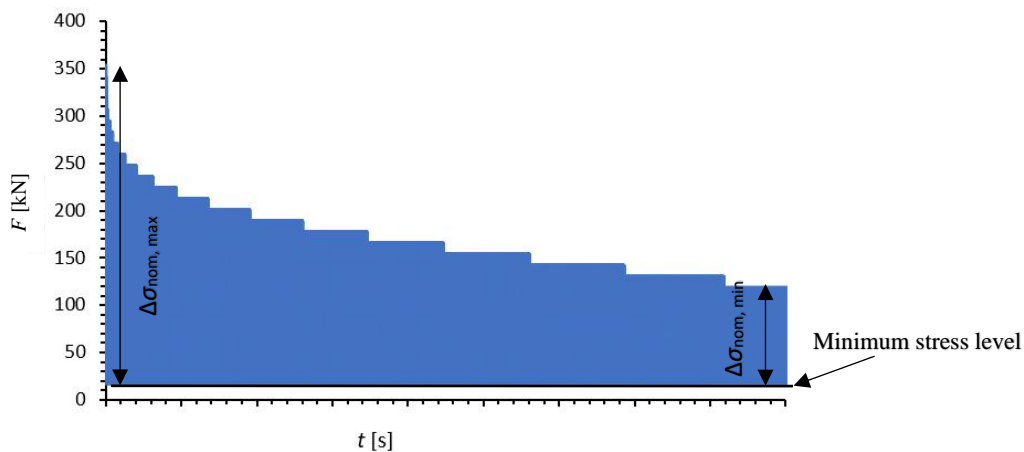
Figure 37. Schematic drawing of the applied gaussian VA loading and calculation points.

The stress ratios were calculated by obtaining the new maximum levels for each block. It was assumed that the minimum loading level would not vary. During the calculation process,

the local stresses caused by the peak load were calculated with equations 13-15. After calculating the first peak load, the differences between the new blocks could be analyzed with equation 14. The calculation of the different stress levels and points can be seen in Figure 37. The damage sum parameter of 1 was used in the calculation and has been recommended by Lipiäinen et al. (2022, p. 13).

4 Results

This section of the thesis presents the experimental fatigue test results with the analytical ones. The focus is on the obtained fatigue strength values of different loading cases and the effect of the applied overload. The strength classes of the welded joints are presented in charts and tables as both nominal and characteristic values with the experimental test results. For comparison, the effect of the pre-applied static overload is evaluated with the results from constant amplitude loading.

The analytical calculations of the fatigue lives and, thus, strength were based on the 4R, nominal stress, ENS and TCD methods. The results were gathered and processed for further evaluations. The differences are shown between the experimentally gathered strength results and the analytically derived ones.

4.1 Numerical finite element analysis results

The stress concentration factors were obtained from the FE models. In the TCD models, both the PM and the LN methods were utilised. Microstructural length of $\rho^* = 0.4$ mm and critical distance of $a = 0.1$ mm were used in the thesis as they have been recommended by Baumgartner et al. (2015). Further analysis was done for the TCD models with the LN method using Equation 4. The calculated stress concentration factors are presented in Table 10 and the maximum principal stresses received from the TCD and ENS models are presented in Figure 38 and Figure 39.

Table 10. The calculated stress concentration factors.

	ENS	TCD (PM)	TCD (LN)
K_m	3.48	3.32	2.34
K_b	3.27	2.81	2.96
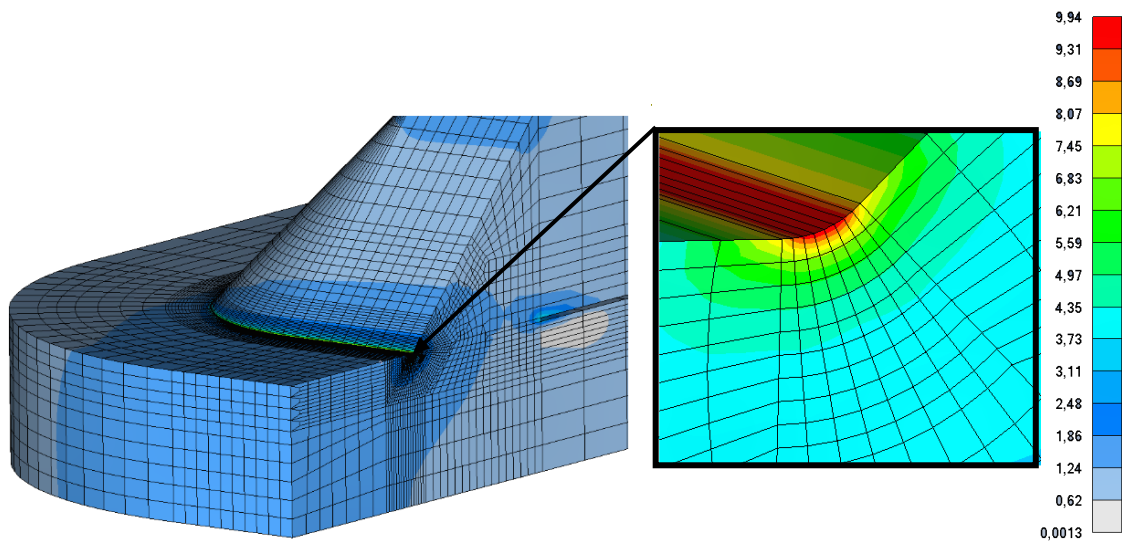
Figure 38. Maximum principal stresses of the TCD model [MPa].
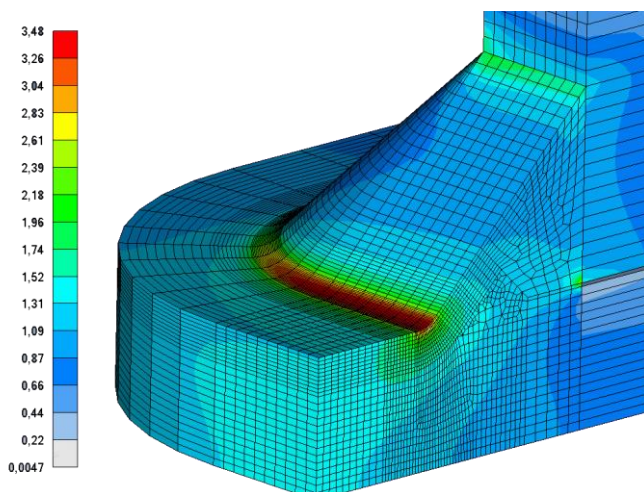
Figure 39. Maximum principal stress values of the ENS model [MPa].

4.2 Fatigue tests

The fatigue tests were conducted for CA, overload and VA loading. The results are vastly presented as S-N curves calculated by different methods and two survival probabilities. The mean values are based on 50 % and characteristic on 97.7 % probability rate. Table 7 presents the test matrix for all steel grades and loading types. The FAT class of 63 MPa provided by IIW (Hobbacher 2016, p. 54) has been modified with a factor of 1.37 to evaluate the fatigue strength for the survival probability of 50 %. The use of coefficient 1.37 has been suggested

by Sonsino et al. (2012, p. 7). The S-N curves were obtained from the fatigue test results (stress and number of cycles) using least square fitting and minimization of sum of squared perpendicular distances (MSSPD). For test series with less than 10 specimens, a fixed slope of 3 has been applied. In the case of the 4R method, purely computational results were obtained with the stress concentration factor calculated by ENS. The S-N curves were created from both the nominal loads and the stress calculated from the strain gage values. The calculation process for the FAT classes is presented in the following equation:

$$FAT = \sqrt[m]{\frac{N_f}{2 \cdot 10^6}} \cdot \Delta\sigma \qquad (19)$$

Where, FAT, is the fatigue classification, m is the exponent of the S-N curve, N_f is cycles to failure and $\Delta\sigma$ is the calculated stress range.

4.2.1 Constant amplitude loading

CA loading was tested with different nominal stress values for the steel grade S700. The fatigue tests resulted in 78 MPa characteristic FAT class with 80 MPa mean value. Derived only from theoretical calculations, the 4R method suggested a slightly higher mean fatigue class of around 105 MPa with a free slope. The S-N curves based on different methods for nominal stresses are presented in Figure 40. Similar S-N curves were derived from the strain gage values and can be seen in Figure 41. The measured strains and HS stresses were calculated according to equation 12. The stresses were higher than the calculated nominal ones suggesting that the specimens had some angular distortion and were subjected to bending. This also led for higher FAT classes. The FAT_{char} and FAT_{mean} values have been obtained from the experimental fatigue test results by using least square fitting, and represent the calculated fatigue classification values for survival probability rates of 97.7 % and 50 %, respectively. These FAT values have been calculated with a fixed slope parameter of 3 due to less than 10 fatigue test specimens. Results from the 4R method have been computed accordingly with the difference of having a free slope parameter.

Figure 40. The S-N curve and calculated FAT classes based on the nominal stress for material S700 under CA loading. Fixed slope of 3 has been applied, for FAT_{char} and FAT_{mean}.
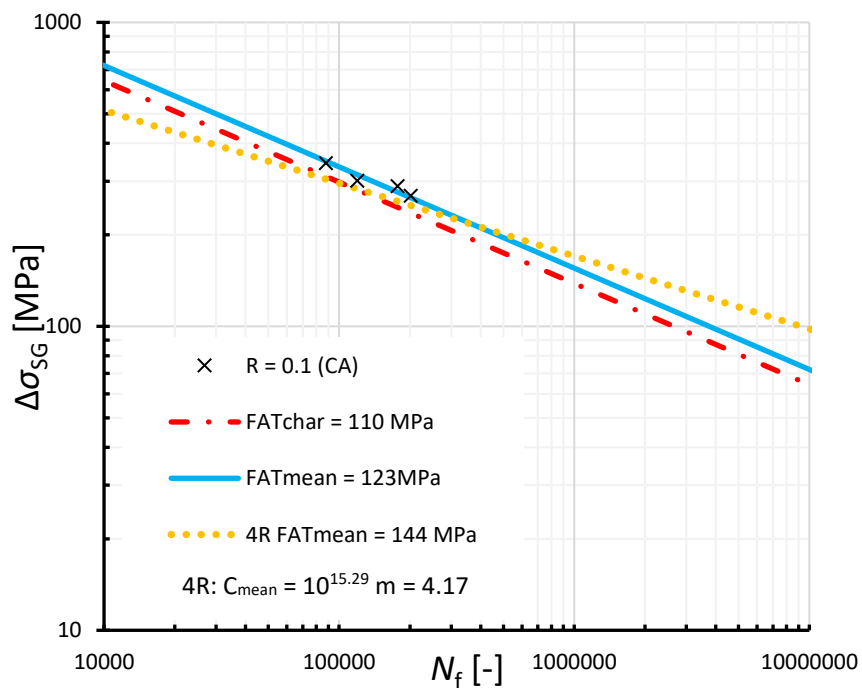
Figure 41. The S-N curve and calculated FAT class based on the strain gage values for S700 and CA loading. Fixed slope of 3 has been applied, for FAT_{char} and FAT_{mean}.

One specimen from this test series experienced weld root failure and others failed from the weld toe. As can be seen from Figure 40, two specimens runout. From these results, the fatigue strength limit can be estimated to be around 125-155 MPa.

4.2.2 Overload level 1

OL1 was applied with CA loading to all steel grades under examination. The level of the static overload was 0.8 YS. The S-N curve from nominal stresses for steel grade S700 can be seen in Figure 42. The overload resulted in a mean FAT class of 129 MPa and a characteristic FAT class of 95 MPa. The nominal mean S-N curve from CA loading is also presented in Figure 42 for comparison. The OL1 resulted in around 1.6 times higher nominal mean FAT class. The S-N curve based on the strain gage values is presented in Figure 43.

Figure 42. The S-N curve and calculated FAT classes based on the nominal stress for material S700 under OL1 and CA loading. Fixed slope of 3 has been applied, for FAT$_{char}$ and FAT$_{mean}$.
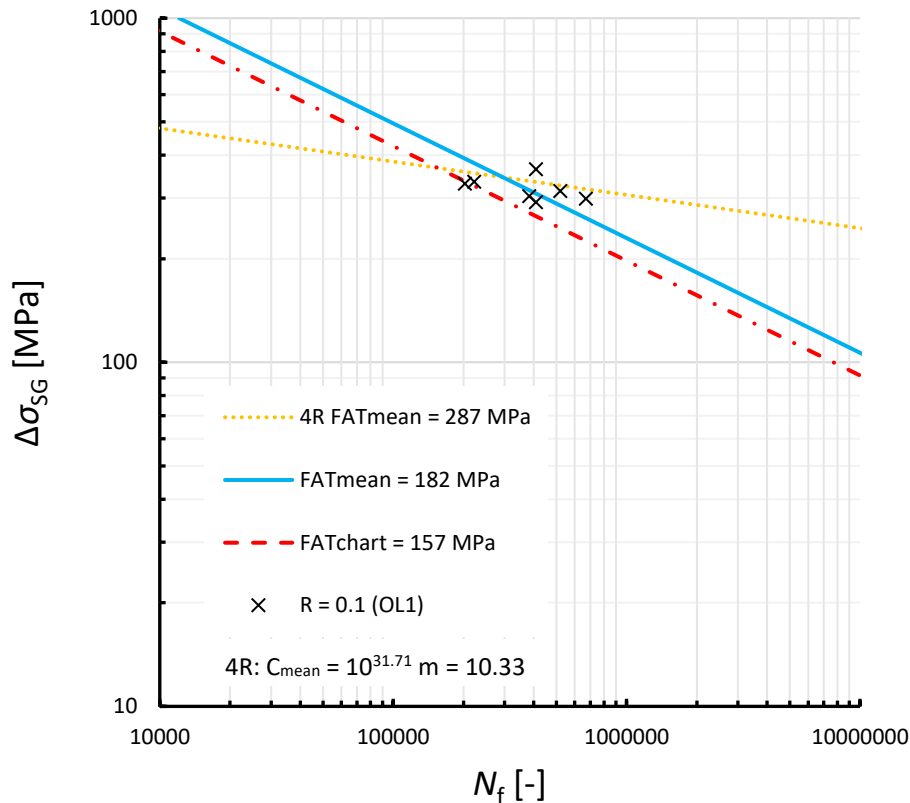
Figure 43. The S-N curve and calculated FAT class based on the strain gage values for S700 under OL1 and CA loading. Fixed slope of 3 has been applied, for FAT_{char} and FAT_{mean}.

The S-N curve for 4R method has been computed with a free slope as opposed to S-N curves derived from the experimental fatigue test results. The 4R method predicted a mean FAT class of 287 MPa with a slope parameter of $m = 10.33$. The prediction had a notably higher FAT class due to not being able to consider the angular distortion of tested specimens and having a free slope parameter in the curve fitting.

The differences in crack growth and propagation between test specimens manufactured of steel grade S700 with and without overload is depicted in Figure 44. The applied nominal stress range was 225 MPa in both fatigue tests and the applied overload was 0.8 YS. The figure was drawn in relation to the measured strains and cycles. The limit of 5 % difference has been used to evaluate the start of the rapid crack growth and the results from OL1 and OL2 are presented in relation to the results from CA loading.
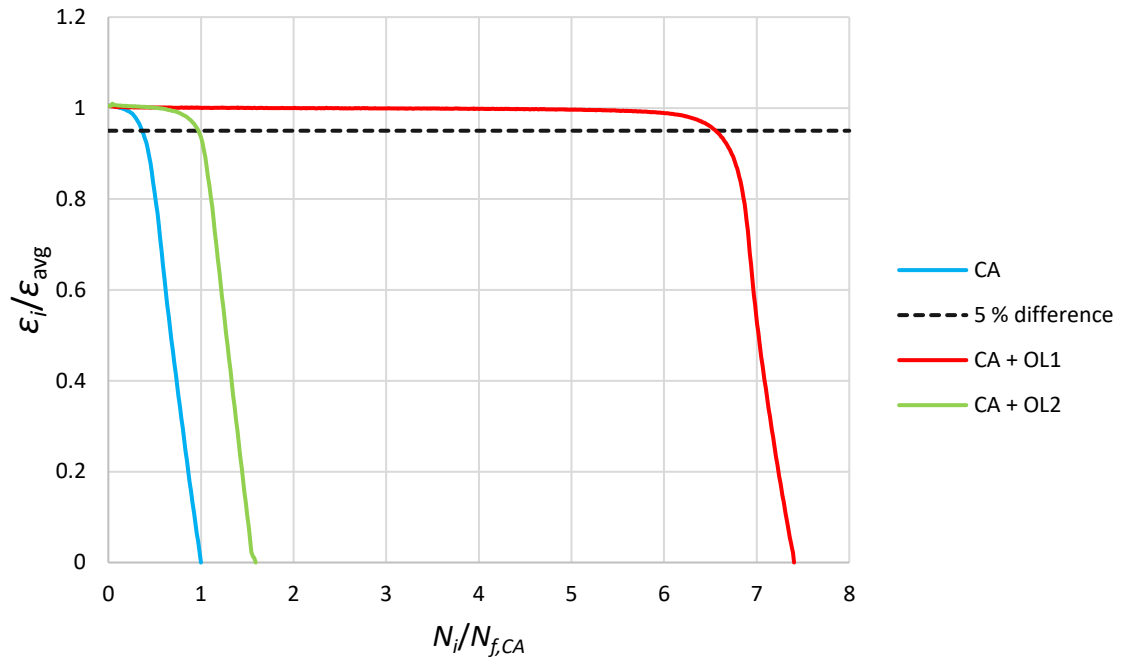
Figure 44. Illustration of the fatigue crack growth between test specimen under CA loading with and without the application of OL1 and OL2.

4.2.3 Overload level 2

OL2 with CA loading was tested only on steel grade S700. Figure 45 presents the S-N curves based on nominal stresses with applied OL2. The application of OL2 resulted in a mean FAT class of 96 MPa and characteristic FAT class of 68 MPa. In comparison with the CA loading, the mean FAT class was approximately 1.2 times higher. There was some deviation in the results as some specimen had higher fatigue strength than others. This can also be seen in Figure 45. The S-N curves were derived using least square fitting and a fixed slope parameter of 3. However, predictions with the 4R method have been made with a free slope parameter.
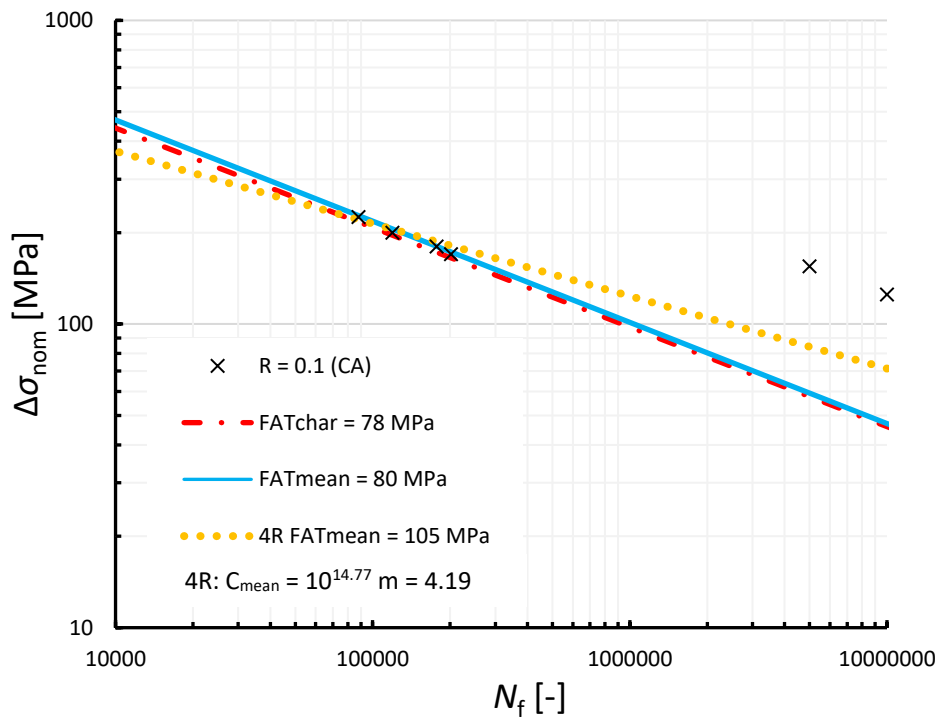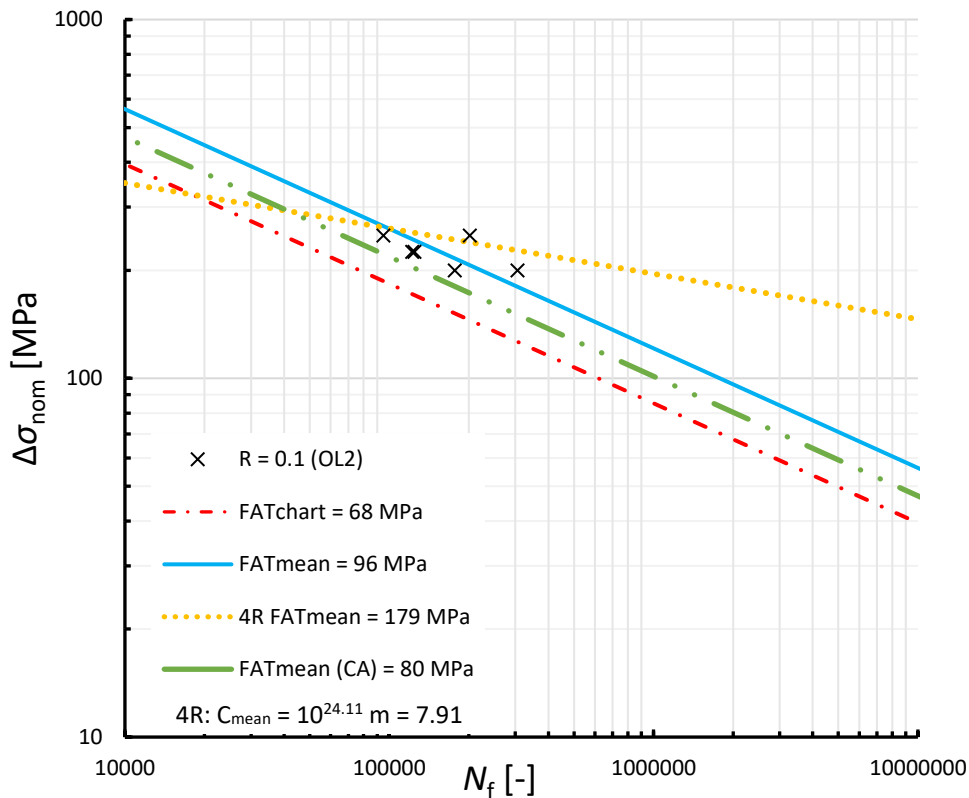
Figure 45. The S-N curve and calculated FAT classes based on the nominal stress for material S700 under OL2 and CA loading. Fixed slope of 3 has been applied, for FAT_{char} and FAT_{mean}.

All tested specimens failed from the weld toe and the tested series did not have runouts. The S-N curves were also derived from experimental strain gage data and can be seen in Figure 46. The mean FAT class based on the strain gage values was 139 MPa and the characteristic one was 109 MPa. In comparison to the results from CA loading, the test specimens with the pre-applied tensile OL2 had slightly higher FAT class. The 4R method predicted higher fatigue strength with a mean FAT class of 179 MPa.
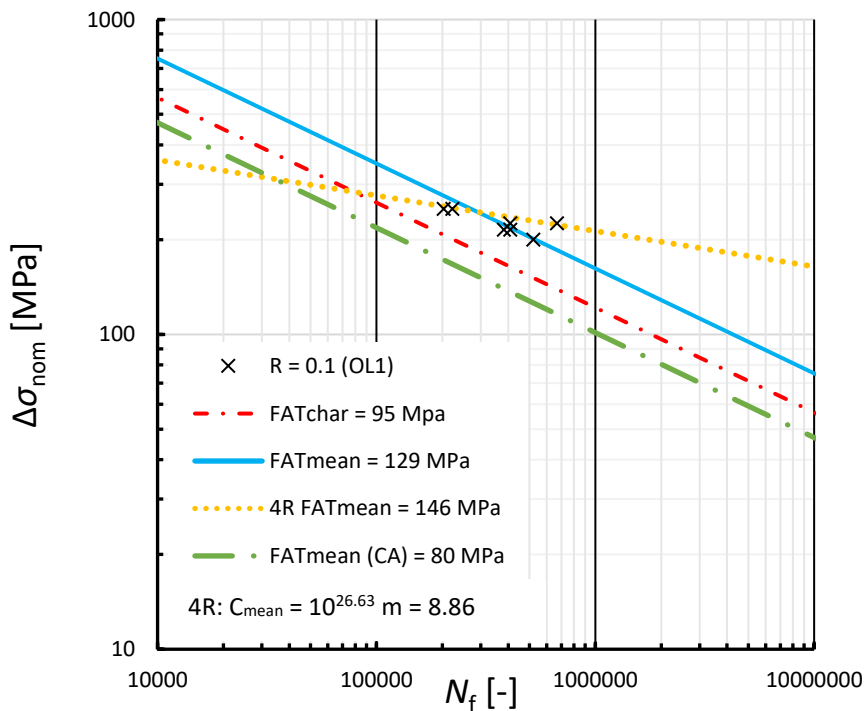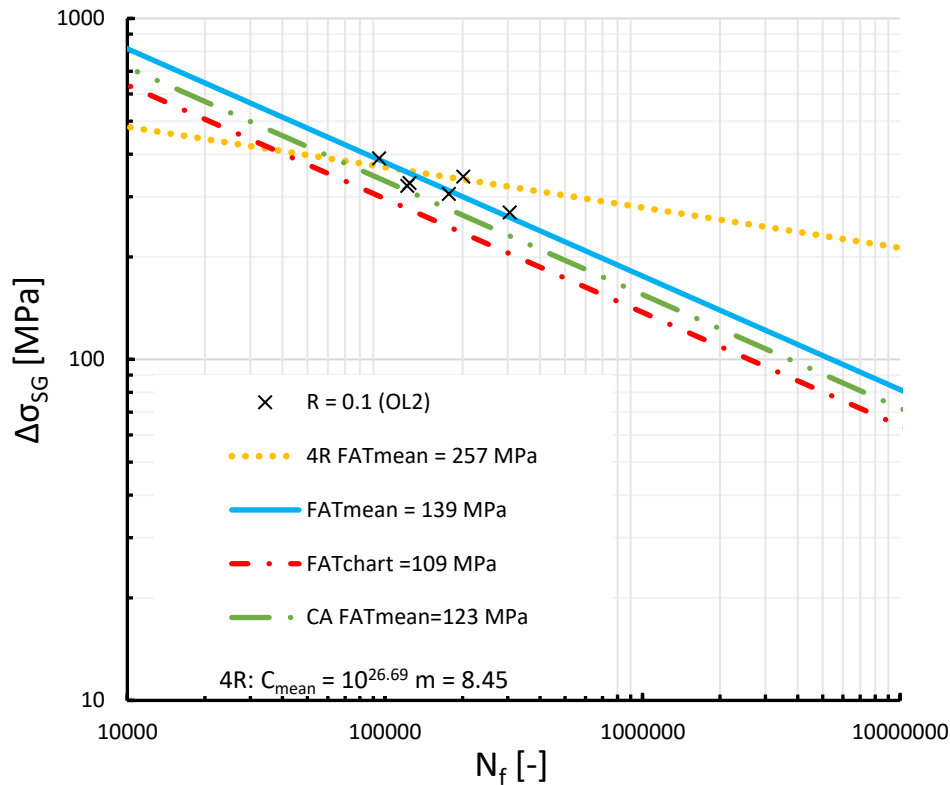
Figure 46. The S-N curve and calculated FAT classes based on the nominal stress for material S700 under OL2 and CA loading. Fixed slope of 3 has been applied, for FAT_{char} and FAT_{mean}.

4.2.4 Variable amplitude loading

Local strain approach, the 4R method was applied to VA loading with steel grade S700. The equivalent stress was calculated with equation 18 considering the local effects. Characteristic FAT class of 225 MPa was used in the fatigue life calculation as it has been recommended by IIW (Hobbacher 2016) and mean FAT class of 308 MPa MPa was derived from the characteristic one using coefficient 1.37. The results presented in Figure 47 contain information obtained from both experimental results and analytical calculations with the 4R method. The S-N curve was derived using least square fitting and a free slope.
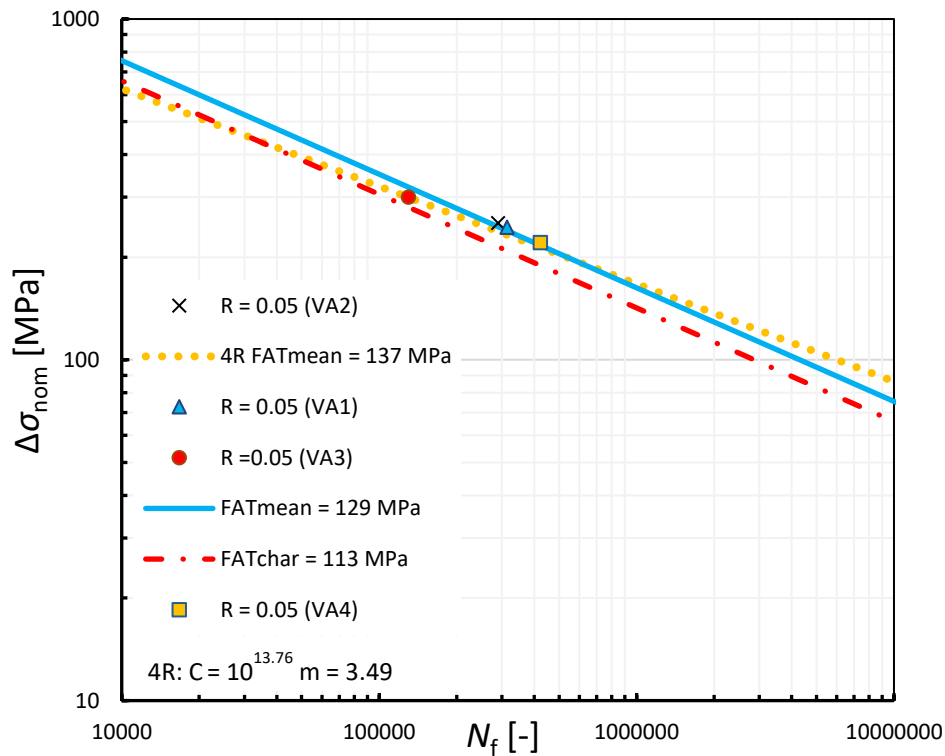
Figure 47. Experimental results from VA loading (S700) and mean S-N curve for the 4R method calculated with ENS. Fixed slope of 3 has been applied, for FAT_char and FAT_mean.

4.3 Residual stresses

One specimen from each test series was selected to be measured and the residual stresses were measured along the centre line of the test specimen starting from the weld toe. Measurements were taken before and after applying the overload. The highest level of overload caused significant relaxation in the residual stresses and resulted even in compression stress along the whole measured length. OL2 relaxed the residual stresses, but the change in residual stresses was not as high as in OL1. The residual stresses for steel grade S700 before and after different overload levels are presented in Figure 48. Residual stresses were also measured in as-welded condition before the HFMI treatment conducted on the other weld toes. It can be noted that the residual stress levels measured after HFMI treatment were of low-level and showed a relaxation near the weld toe.
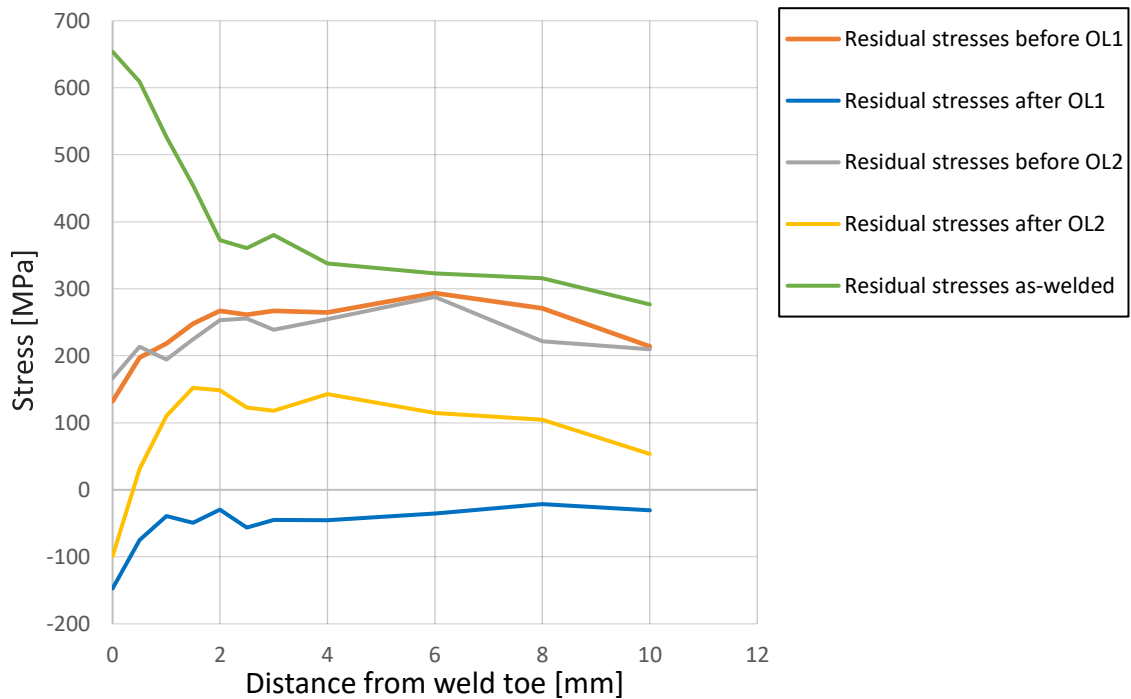
Figure 48. Residual stresses from steel grade S700 before and after OL1 and OL2.

Residual stresses were also measured for steel grades S355 and S1100 before and after the application of the overload. Only OL1 was tested and measured for the control group. For comparison, the residual stresses were also obtained in as-welded condition before the HFMI treatment. The measured residual stresses for steel grades S355 and S1100 are presented in Figure 49. The results show that for steel grade S1100 the OL1 induced major compressive residual stresses along the measured length with -335 MPa minimum stress value.

For steel grade S355, the HFMI treatment on the opposite side of the base plate notably relaxed the residual stresses on the weld toe. It had, however, lower impact as the distance increased further along the measured line and away from the weld toe. Moreover, in the case of S355 the OL1 did not notably relax the residual stresses in the weld toe after the HFMI but affected the base plate along the measured length.
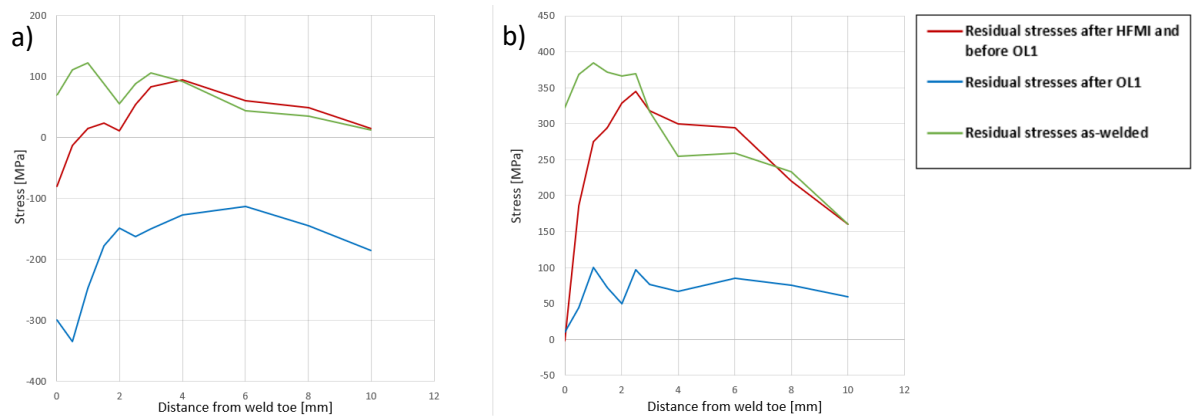
Figure 49. Residual stresses for steel grade S1100 (a) and S355 (b).

4.4 3D measurements of the test specimen

At least one specimen from each series was scanned with a 3D measurement device to identify the shape and sizes of the welded joint. One specimen of steel grade S700 was examined further with a profilometer to better detect the weld toe radius. The typical weld shape and weld toe radius are presented in Figure 50. The scanned specimens each had a throat thickness of approximately 4 mm and the weld toe radii were between 0.1-0.3mm. The throat thicknesses were estimated by fitting a curve through measured points. The weld shapes had variation and were not symmetrical. There were also some spatters near the weld toe and on the base plate.
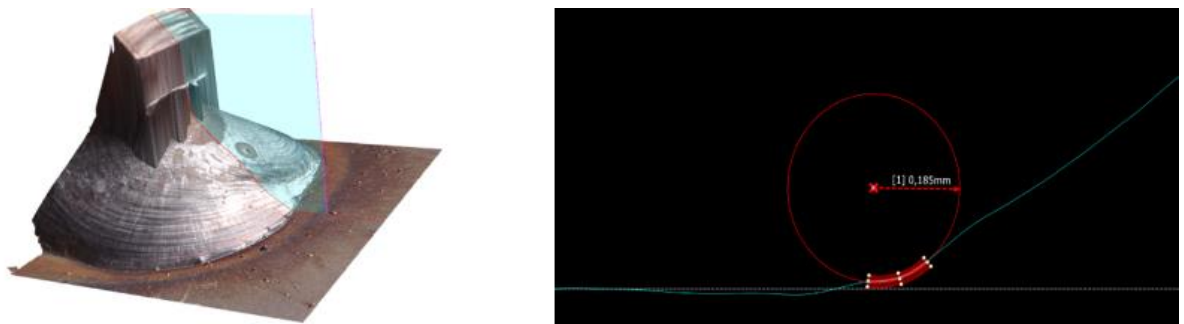
Figure 50. Scanned weld shape of a S700 test specimen.
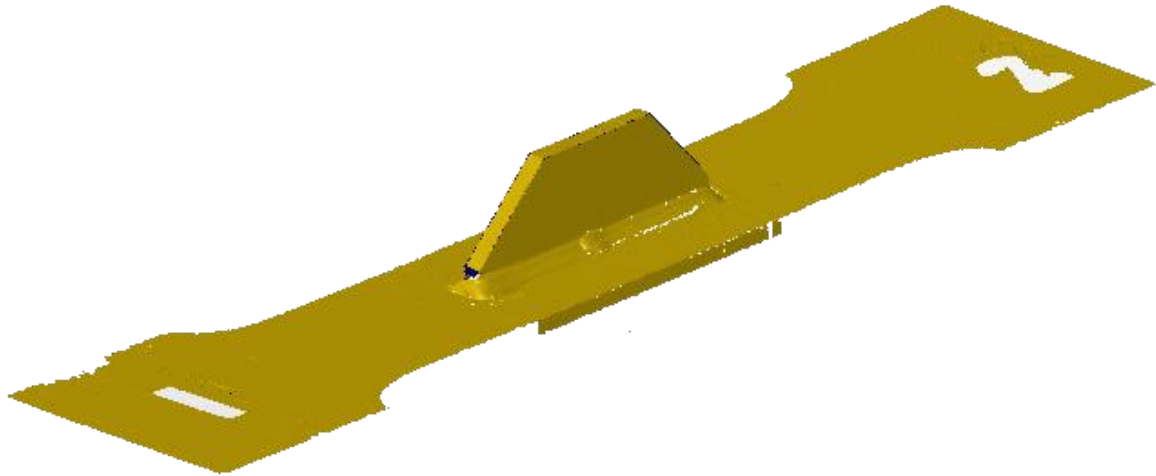
Figure 51. Overall view of a 3D scanned specimen and its weld.

Polished cross-sections were also made from one test specimen manufactured of steel grade S700. Macro figures from both the weld toe are and full cross section were taken. Furthermore, hardness was measured from the weld toe area and the results are presented in with the macro figures in Appendix VI. The polished cross sections did not show any critical welding defects. Hardness measurements showed some softening near the weld toe that could have an impact on the fatigue strength and location of the failure.

4.5 Analytical calculations

Analytical calculations were made using different methods such as the nominal stress, ENS and 4R methods. In this section, the fatigue strength evaluations based on literature and the stress concentration factors obtained with FE analysis are presented. R-O material models are also illustrated with different 4R parameters and material S700. The estimations for fatigue classifications based on the nominal stress and HS stress were obtained from the IIW recommendations by Hobbacher (2016) and are presented in Table 11. To receive the mean values of the characteristic FAT values, a coefficient of 1.37 was applied. This coefficient has been recommended in a research article by Sonsino et al. (2012, p. 7).

Table 11. The fatigue classifications based on different methods. The characteristic values have been estimated with a 1.37 coefficient. (Hobbacher 2016, p. 54-62)

	Nominal [MPa]	HS [MPa]	ENS [MPa]
FAT_{char}	63	90	225
FAT_{mean}	86	123	308

Experimental fatigue test results for steel grade S700 were compared to the computational, theoretical results received with the TCD (PM) and 4R method. These are presented in Figure 52. The computational results were vastly non-conservative. The material parameters presented in Table 8 for R-O material model and Neuber's hyperbolae are presented in Figure 53. The figures were drawn with values for steel grade S700. It can be seen that there is deviation between the two set of parameters and that $H = 1.6\ R_m$ and $n = 0.15$ give lower stress values. This suggests that the material values which lead to lower mean stress also estimate higher fatigue strength values.
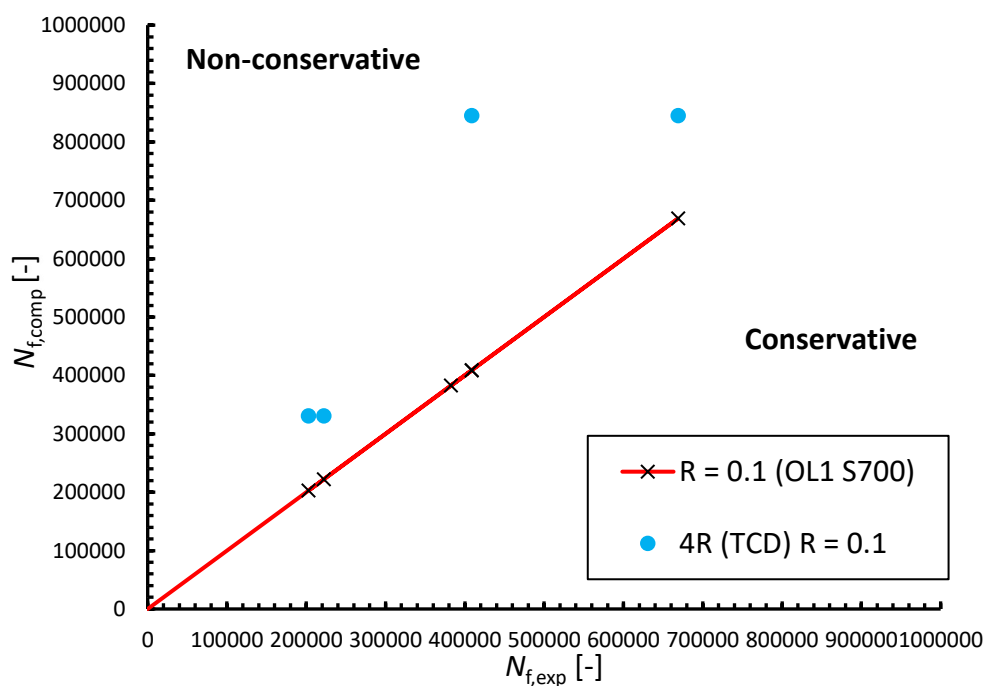
Figure 52. Experimental fatigue test results for steel grade S700 in comparison with calculated results from the 4R method with TCD (PM).
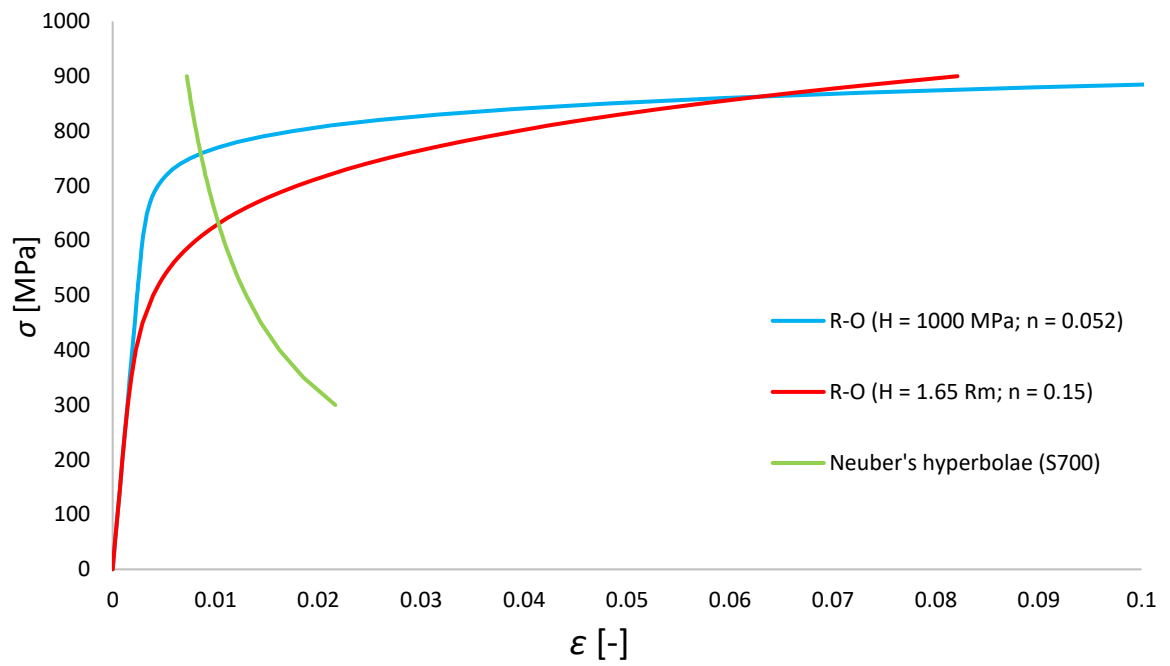
Figure 53. R-O material model with different parameters and Neuber's hyberbolae. The figures were drawn for steel grade S700.

5 Discussion

In this thesis, overload and VA load effects on the fatigue strength of welded joints were studied by utilising experimental fatigue testing and analytical calculations. The welded joint under investigation was a longitudinal NLC joint with a double gusset. Other joint types were not considered. Main material in the study was steel grade S700. Steel grades S355 and S1100 were acting as a control group. Two different overload levels (OL1 and OL2) were applied in the fatigue tests with CA loading to examine the possible correspondence. The higher level of overload was 0.8 of YS and lower 0.6 of YS. Experimental tests were also conducted on VA loading with block type loading. The VA loading was designed to include a high peak load and series of descending, lower cycles. The main computational tools included were the 4R, ENS, TCD and nominal stress method. FE analysis was used to obtain the stress concentration factors from the weld toe. The key topics of interest were the potential differences caused by the overload in the fatigue strength and local residual stresses with respect to results from CA loading. Differences between steel grades were also of interest. Furthermore, the use of 4R method was evaluated to both overload and VA cases.

Overall, 39 fatigue tests were conducted on welded joints. A strain gage was inserted to each specimen to measure strain data. Detailed lists of results with specimen IDs are presented in Appendix III. S-N curves were created based on the results for the main material and are presented in Section 4. Results of the control groups are presented and analysed in Section 5.1. For steel grade S700, the individually applied tensile OL1 improved the fatigue strength significantly. In comparison with the results from CA testing, the mean FAT class calculated from nominal stresses was approximately 1.6 times higher. OL2 had less impact on the fatigue strength but did improve the corresponding mean FAT class with a factor of 1.2. Computational results for VA loading using the 4R method are presented in Section 4.1.4.

5.1 Analysis of fatigue test results

For control groups S1100 and S355, single tensile OL1 with CA loading was applied. The S-N curves for the above materials are presented in Figure 54 and Figure 55. The S-N curves

were derived using least square fitting and had a fixed slope of 3Steel grade S1100 benefited most from the tensile overload in the form of fatigue strength as it had a mean FAT value of 151 MPa considering nominal stresses. In the case of steel grade S700, the mean FAT value for OL1 specimens was 129 MPa. These differences can be seen in Figure 54. When CA results are compared from S700, it can be noted that the OL1 results for S1100 are approximately 1.9 times higher. These results appear reasonable considering the local strain effects and compressive residual stresses caused by the overload. The effect of HFMI from the opposite side of the base plate should also be considered, as X-ray residual stress measurements show a connection between lowered values and the post-process itself.

Notch approach 4R method predicted a significantly higher improvement with mean FAT class of 294 MPa and was able to take into consideration the local behaviour in the weld. This phenomenon is illustrated in Figure 36. Traditional and most common fatigue calculation methods do not cover these aspects and suggest distinctly conservative FAT values. These values are presented more thoroughly in Section 4.4. The TCD method predicted also low stress concentration factors in comparison with the ENS method and when applied to fatigue life calculations provided even more highly non-conservative results.
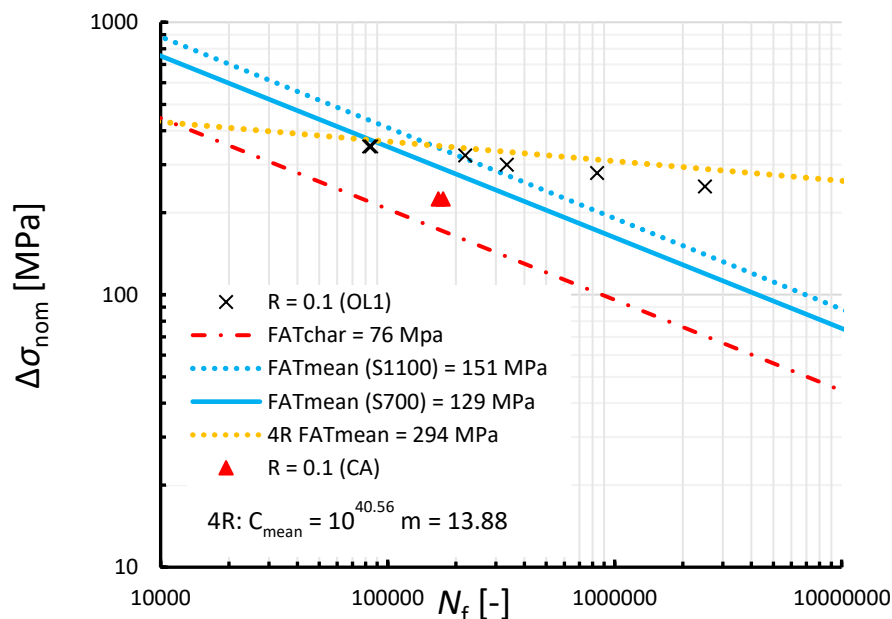
Figure 54. S-N curves for steel grade S1100 with OL1. The OL1 results from S700 with OL1 are shown for comparison. Fixed slope of 3 has been applied, for FAT_{char} and FAT_{mean}.

Steel grade S355 did not have as high of an improvement fatigue strength wise as did the other tested materials. S355 had a mean FAT value of 92 MPa for specimens with OL1 and CA loading. In comparison with CA fatigue test results from S700, the fatigue strength was, however, moderately improved with a factor of 1.15 in terms of mean FAT values. The difference between materials S700 and S355 with OL1 can be seen in Figure 55. The 4R method predicted higher mean FAT value of 133 MPa being vastly optimistic. The lower fatigue strength could be due to higher residual stress levels and having less plasticity. As can be seen from the residual stress results in Figure 49, the residual stresses did not go into compression for steel grade S355 despite the 0.8 YS overload. Theoretically, the lower level of improvement in the fatigue strength could be caused by too high CA loadings as stress range of 225 MPa would reach 0.63 YS for S355. High mean stress values in CA loading would cause the overload to have less of an effect on the results.
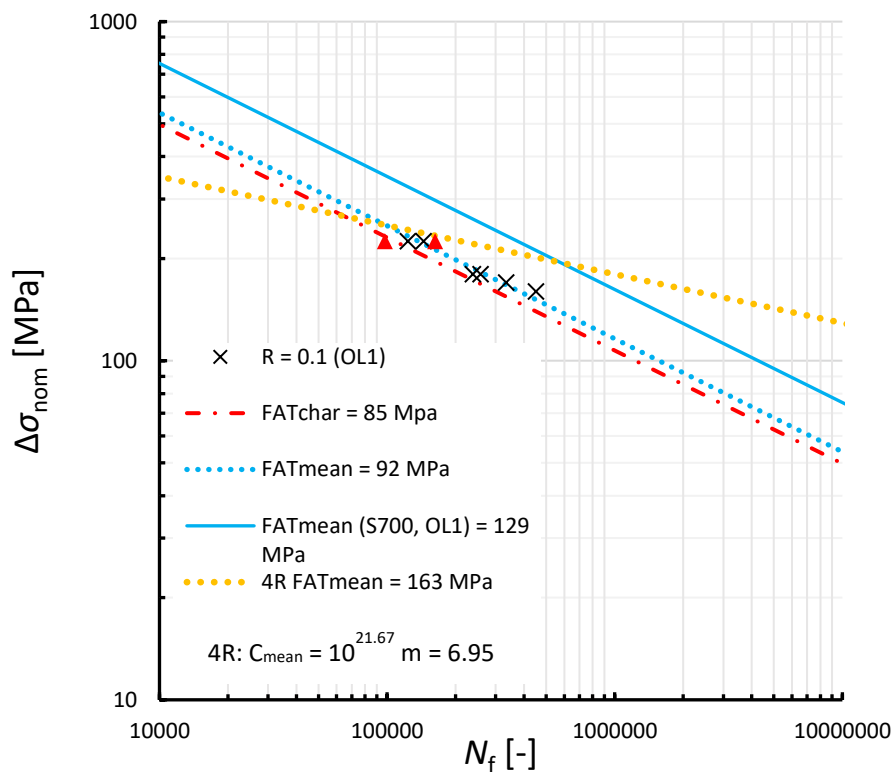
Figure 55. S-N curves for steel grade S355 with OL1 and CA loading. The OL1 results from S700 are shown for comparison. Fixed slope of 3 has been applied, for FAT_{char} and FAT_{mean}.

The fatigue test results were also analysed with respect to the mean stress corrected reference stress calculated with the 4R method and ENS. These results can be seen in Figure 56. The S-N curve was derived from the experimental fatigue test results using MSSPD and a free slope. The calculated mean and characteristic FAT classes were 296 MPa and 177 MPa, respectively. As can be seen in Figure 56, for steel grade S700, the CA results were best fitted on the curve. Steel grade S355 had also, only, small deviation from the mean curve. Steel grade S1100 resulted in lower stress values considering the mean stress correction and local stress ratio. The slope parameter was lower when compared to the purely theoretical estimations with the 4R depicted in the nominal stress range. This could be due to factors including differences between theoretical calculations and experimental fatigue test results or changes that were caused by higher stress values than the nominal ones.
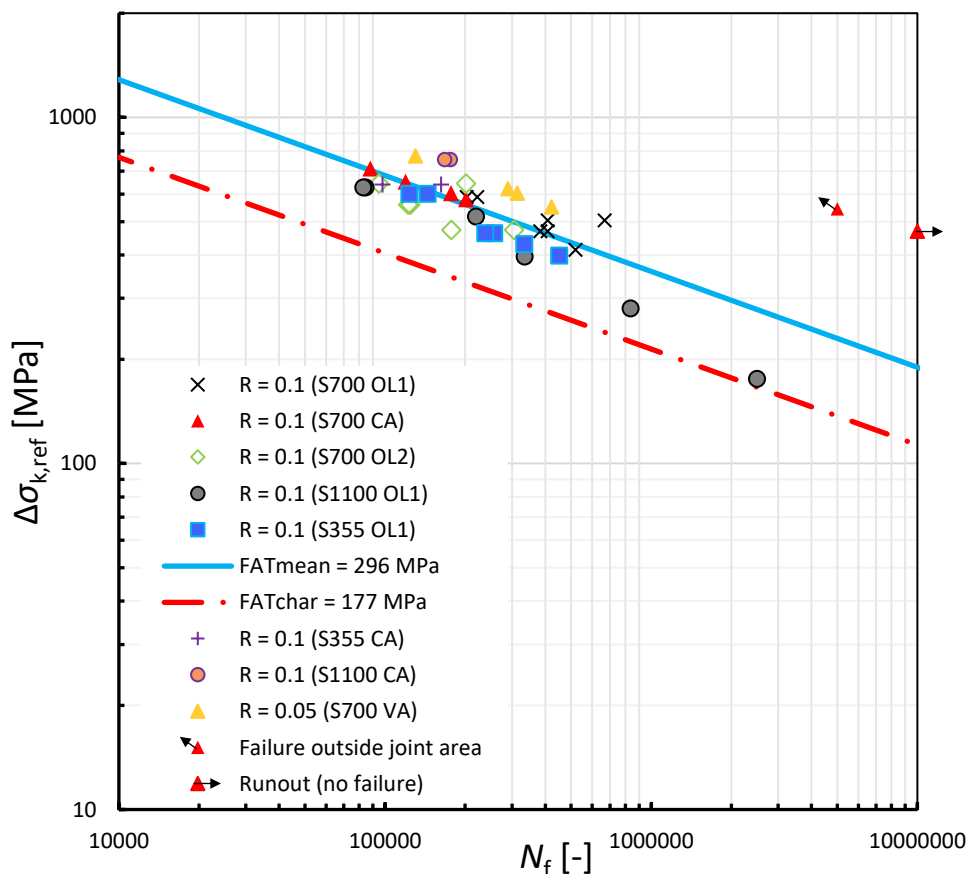
Figure 56. Experimental fatigue test results in terms of the mean stress corrected reference stress. S-N curve parameters are $m_{free} = 3.61$ and $C_{mean} = 10^{15.23}$.

5.2 Topics for further research

Application of a single tensile overload increased the fatigue strength in the welded joint was studied in this thesis. It was noted that OL1 had a more significant effect in comparison with the lower level, OL2. Further research topics could include studying the same effect on various welded joint types and on different materials. Welded joints could include cruciform, butt or lap joints. Furthermore, the fatigue tests should be conducted with more extensive testing to ensure the reliability and validity of the results. In this thesis, each test series included 6-7 test specimens manufactured of steel grades S700, S355 and S1100. More fatigue tests would be necessary to evaluate the slope of the S-N curves reliably.

The 4R method gave reasonable but slightly optimistic estimations for the OL cases. More research could also be conducted on the effects of different parameters and the calculation method itself to further improve it. Implementation of the TCD to the 4R method and analysis of overload and VA cases of welded joints could also be studied more. Moreover, fatigue testing of VA loading should be performed more extensively to make conclusions on the computational methods and their applicability. The TCD method and its initial parameters, critical and microstructural length, could also be examined for most optimal results as the results from this study indicate non-conservative values for the stress concentration factor.

In the residual stress measurements, it was noticed that the HFMI had a significant effect on the stress levels in the weld toe for all steel grades despite being implemented only on the opposite side of the base plate. This correlation could be further investigated in applications where post-processing is not possible in the weld toe directly. The topic of interest could in that case be the effect of HFMI treatment from the other side of a steel plate or from a distance along the base plate.

5.1 Conclusions

Fatigue strength of welded joints under overloads and VA loading was investigated. The key methods included fatigue testing and analytical calculations. Based on the study the following conclusions were drawn:

- The fatigue strength of the investigated welded joint was improved when a single tensile overload was applied before fatigue tests. Improvement of different levels was noticed for all studied steel grades and overloads.

- The higher-level overload (OL1) resulted in 1.6 times higher FAT class for material S700 in comparison with traditional CA loading.

- The lower-level overload (OL2) had less effect on the fatigue strength than OL1. It did, however, result in 1.2 times higher FAT class for material S700 in comparison with traditional CA loading.

- From the fatigue strength improvement viewpoint, steel grade S1100 benefited most from the overload as the fatigue strength was improved by a factor of 1.9 when compared to CA results from S700. Material S355 had least improvement.

- The application of overload relaxed the residual stresses and created new ones that were on the compression side. The residual stress results were, however, affected by the HFMI treatment on the opposite side of the base plate.

- Traditional fatigue life calculation methods do not consider the local stress and strain behaviour of the welded joint under overloads. This leads to overly conservative FAT classes and predictions in the case of pre-applied tensile overloads.

- For OL cases, the 4R method was able to consider the local material model and stresses and estimated the experimental fatigue lives with more precision. It was, however, slightly on the non-conservative the side which could be due to features such as bending stress caused by angular distortion, welding defects or errors in residual stress measurements. The material parameters could also be more optimized.

- For cases with VA loading, the 4R method with ENS gave reasonable predictions of the fatigue strength and lives. The predictions were slightly on the conservative side and provided better estimations in comparison with the conventional methods.

- The TCD method with critical distance of 0.1 lead to lower stress concentration factors than the ENS method. The results indicated that use of TCD leads to highly non-conservative fatigue life calculation results.

References

Ahola, A., Skriko, T., Björk, T. 2019. Fatigue strength assessment of ultra-high-strength steel fillet weld joints using 4R method. Journal of Constructional Steel Research, 167. P. 1-12. https://doi.org/10.1016/j.jcsr.2019.105861.

Amraei, M., Zhao, X., Ahola, A., Afkhami, S., Björk, T., Heidarpour, A. 2019. Effects of heat input on the mechanical properties of butt-welded high and ultra-high strength steels. Engineering Structures, 198. P. 1-15. https://doi.org/10.1016/j.engstruct.2019.109460.

ASTM A391 / A391M-07. 2012. Standard Specification for Grade 80 Alloy Steel Chain.

Baumgartner, J., Hobbacher, A., Rennert, R. 2020. Fatigue assessment of welded thin sheets with the notch stress approach – Proposal for recommendations. International Journal of Fatigue, 140. P. 1-14. https://doi.org/10.1016/j.ijfatigue.2020.105844.

Baumgartner, J., Schimdt, H., Ince, E., Melz, T., Dilger, K. 2015. Fatigue assessment of welded joints using stress averaging and critical distance approaches. Welding in the World, 59. P. 731–742.

Baumgartner, J & Bruder, T. 2013. An efficient meshing approach for the calculation of notch stresses, Welding in the World. 57 (1). P. 137–145.

Björk, T., Mettänen, H., Ahola, A., Lindgren, M., Terva, J. 2018. Fatigue strength assessment of duplex and super-duplex stainless steels by 4R method. Welding in the World, 62. P. 1285–1300. https://doi.org/10.1007/s40194-018-0657-8.

Carpinteri, A., Spagnoli, A., Vantadori, S. 2017. A review of multiaxial fatigue criteria for random variable amplitude loads. Fatigue & Fracture of Engineering Materials & Structures, 40. P. 1007–1036.

ESAB. 2023a. Internet source. Referenced [15.02.2023]. Available: https://esab.com/kh/apc_en/products-solutions/product/filler-metals/covered-stick-electrodes-smaw/stainless-steel-electrodes/ok-69-25/

ESAB. 2023b. Internet source. Referenced [16.02.2023]. Available: https://esab.com/sa/mea_en/products-solutions/product/filler-metals/mig-mag-wires-gmaw/mild-steel-wires/ok-autrod-12-51/

Fricke, W. 2010. Guideline for the fatigue assessment by notch stress analysis for welded structures. International institute of welding. IIW-Doc. XIII-2240r2-08/XV-1289r2-08. P. 1-38.

Fricke, W. 2013. IIW guideline for the assessment of weld root fatigue. Welding in the world, 57. P. 753–791.

Fällgren, C., Beier, T., Vormwald, M., Kleemann, A. 2021. Autofrettage of component-like ultra-high strength steel specimens with intersecting holes. Procedia Structural Integrity, 37. P. 948-955. https://doi.org/10.1016/j.prostr.2022.02.030.

González, P., Cicero, S., Arroyo, B., Álvarez, J.A. 2019. A Theory of Critical Distances based methodology for the analysis of environmentally assisted cracking in steels. Engineering Fracture Mechanics, 214. P. 134-148. https://doi.org/10.1016/j.engfracmech.2019.04.004

Hemmesi, K., Ellmer, F., Farajian, M., Varfolomeev, I., Luke, M. 2022. On the evaluation of overload effects on the fatigue strength of metallic materials. Procedia Structural Integrity, 38(C). P. 401–410. https://doi.org/10.1016/J.PROSTR.2022.03.041.

Hobbacher, A. 2016. Recommendations for fatigue design of welded joints and components. Second edition. IIW collection.

Huther, I., Lefebvre, F., Abdellaoui, B., Leray, V. 2022. Influence of over-load on fatigue behaviour of longitudinal non-load-carrying welded joints. Procedia Structural Integrity, 38. P. 466-476. https://doi.org/10.1016/j.prostr.2022.03.047.

Köhler, M., Jenne, S., Pötter, K., Zenner, H. et al. 2017. Load Assumption for Fatigue Design of Structures and Components Counting Methods, Safety Aspects, Practical Application. Berlin, Heidelberg: Springer Berlin Heidelberg.

Liang, H., Zhan, R., Wang, D., Deng, C., Guo, B., Xu, X. 2022. Fatigue crack growth under overload/underload in different strength structural steels. Journal of Constructional Steel Research, 192. P. 1-18. https://doi.org/10.1016/J.JCSR.2022.107213.

Lipiäinen, K., Ahola, A., Björk, T. 2022. Fatigue performance of hot-dip galvanized ultra-high-strength steel laser cut notches under constant and variable amplitude loading (IIW doc. XIII-2934-2022). IIW document, Tokyo. P. 1-15.

Lu, Y., Yang, F., Chen, T. 2019. Effect of single overload on fatigue crack growth in QSTE340TM steel and retardation model modification. Engineering Fracture Mechanics, 212. P. 81-94.

Mizukami, H., Hanaori, K., Takahashi., K., Tange, A., Ando, K. 2010. Improvement fatigue limit of steel containing a small crack-like surface defect by overload effect. International Journal of Structural Integrity, 1. P. 153–160.

Niemi, E., Fricke, W., Maddox, S. J. 2006. Fatigue Analysis of Welded Components: Designer's Guide to the Structural Hot-Spot Stress Approach. Cambridge, United Kingdom: Woodhead Publishing Ltd. P. 11-13.

Nussbaumer, A., Borges, L., Davaine, L. 2018. Fatigue design of steel and composite structures: Eurocode 3: design of steel structures, part 1-9 fatigue, Eurocode 4: design of composite steel and concrete structures. Newark: WILEY.

Nykänen, T., Mettänen, H., Björk, T., Ahola, A. 2017. Fatigue assessment of welded joints under variable amplitude loading using a novel notch stress approach. International Journal of Fatigue, 101:2. P. 177-191.

Rohani Raftar, H., Dabiri, E., Ahola., A., Björk, T. 2022. Weld root fatigue assessment of load-carrying fillet welded joints: 4R method compared to other methods. International Journal of Fatigue, 156. P. 1-11.

Sahu, V. K., Anil, Kumar, J.K.S., Mohanty, J.R., Verma, B.B., Ray, P.K. 2014. Effect of low-temperature overload on fatigue crack growth retardation and prediction of post overload fatigue life. Aerospace Science and Technology, 33. P. 100–106. http://dx.doi.org/10.1016/j.ast.2014.01.005

SFS-EN 1011-1. 2009. Welding. Recommendations for welding of metallic materials. Part 1: General guidance for arc welding.

SFS-EN 1011-2. 2004. Welding. Recommendations for welding of metallic materials. Part 2: Arc welding of ferritic steels.

Simunek, D., Leitner, M., Grün, F. 2018. In-situ crack propagation measurement of high-strength steels including overload effects. Procedia Engineering, 213. P. 335–345. https://doi.org/10.1016/j.proeng.2018.02.034

Sonsino, C. M., Fricke, W., De Bruyne, F., Hoppe, A., Ahmadi, A., Zhang, G. 2012. Notch stress concepts for the fatigue assessment of welded joints – Background and applications. International Journal of Fatigue, 34. P. 2–16.

SSAB. 2023a. Internet source. Referenced [15.02.2023]. https://www.ssab.com/en/brands-and-products/ssab-domex/product-offer/355mc

SSAB. 2023b. Internet source. Referenced [15.02.2023]. Available: https://www.ssab.com/en/brands-and-products/strenx/product-offer/700/mc-plus
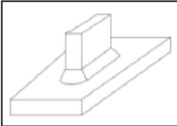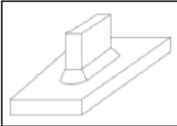
SSAB. 2023c. Internet source. Referenced [15.02.2023]. Available: https://www.ssab.com/en/brands-and-products/strenx/product-offer/1100/mc

Taylor, D. 2007. The Theory of Critical Distances a New Perspective in Fracture Mechanics. Elsevier, 2007. 307. ISBN 1-281-07670-8.
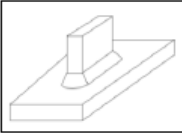
Voestalpine. 2023. Internet source. Referenced [11.4.2023]. Available: https://www.voestalpine.com/highperformancemetals/cs/app/uploads/sites/18/2019/03/B%C3%B6hler-Welding-Produktkatalog-EN-2019-1.pdf

Weich, I., Ummenhofer, T., Nitschke-Pagel, T., Dilger, K., Eslami Chalandar, H. 2009. Fatigue Behaviour of Welded High-Strength Steels after High Frequency Mechanical Post-Weld Treatments. Welding in the World, 53. P. 322–332.
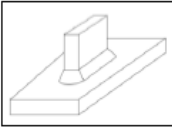
Appendix I: Welding procedure specifications.

pre Welding Procedure Specification   pWPS

Parent material	SSAB Strenx 700 MC Plus		
Material thickness	8 mm	Joint type	Welding sequences
Outside diameter	-		
Welding process	GMAW		
Welding position	2F		
Groove preparation	-		
Groove cleaning	Wire brush		
Workpiece fixturing	Clamped		
Tack welding	3 tack welds on the sides		
Back gouging	-		
Backing	-		

	Designation of consumables and trade name	Torch angle	45 deg
Filler material classification	SFA/AWS A5.4 : E316LMn-15	Inclination angle	5 deg
	EN ISO 3581-A : E 20 16 3 Mn N L B 4 2	Distance contact tube to workpiece	18 mm
		Preheating and interpass temperature	
Filler material trade name	OK 69 Esab	Preheat temperature	No (ambient)
		Interpass temperature	-
Flux		Preheating method	Ambient air
Shielding gas	Argon + 8 % CO_2	Temperature measurement	Pyrometers
Flow rate	14 l/min	Post-weld heat treatment	
Plasma gas	-	Method	-
Flow rate	-	Heating rate	-
Backing gas	-	Temperature	-
Flow rate	-	Time	-
Type of current	DC+	Cooling rate	-
Polarity		Post-weld treatment	Hiflt, HFMI treatment

Remarks:	Date and name:

Run	Process	Size of filler metal Ø (mm)	Current (A)	Voltage (V)	Travel speed (mm/min)	Wire feed rate (m/min)	Heat input (kJ/mm)	Run-out length (mm)	Weaving frequency (Hz)	Amplitude (mm)	Remarks
1	GMAW	1	213-228	26-27	7.8	11	0.57-0.61				
2	GMAW	1	213-228	26-27	7.8	11	0.57-0.61				
3	GMAW	1	213-228	26-27	7.8	11	0.57-0.61				
4	GMAW	1	213-228	26-27	7.8	11	0.57-0.61				

Appendix I: Welding procedure specifications.

pre Welding Procedure Specification   pWPS

Parent material	SSAB Domex 355 MC		
Material thickness	8 mm	Joint type	Welding sequences
Outside diameter	-		
Welding process	GMAW		
Welding position	2F		
Groove preparation	-		
Groove cleaning	Wire brush		
Workpiece fixturing	Clamped		
Tack welding	3 tack welds on the sides		
Back gouging	-		
Backing	-		

	Designation of consumables and trade name	Torch angle	45 deg
Filler material classification	SFA/AWS A5.18 : ER70S-6	Inclination angle	5 deg
	EN ISO 14341-A : G 38 3 C1 3Si1 EN ISO 14341-A : G 42 4 M20 3Si1 EN ISO 14341-A : G 42 4 M21 3Si1 EN ISO 14341-A : G 3Si1	Distance contact tube to workpiece	18 mm
	CSA W48 : B-G 49A 3 C1 S6	Preheating and interpass temperature	
Filler material trade name	OK Autorod 12.51 Esab	Preheat temperature	No (ambient)
		Interpass temperature	Ambient air
Flux	-	Preheating method	-
Shielding gas	Argon + 8 % CO_2	Temperature measurement	Pyrometer
Flow rate	14 l/min	Post-weld heat treatment	
Plasma gas	-	Method	-
Flow rate	-	Heating rate	-
Backing gas	-	Temperature	-
Flow rate	-	Time	-
Type of current	DC+	Cooling rate	-
Polarity		Post-weld treatment	Hiflt, HFMI treatment

Remarks: Date and name:

Run	Process	Size of filler metal Ø (mm)	Current (A)	Voltage (V)	Travel speed (mm/min)	Wire feed rate (m/min)	Heat input (kJ/mm)	Run-out length (mm)	Weaving frequency (Hz)	Amplitude (mm)	Remarks
1	GMAW	1	223-228	26.8-27.1	7.8	11	0.62-0.63				
2	GMAW	1	223-228	26.8-27.1	7.8	11	0.62-0.63				
3	GMAW	1	223-228	26.8-27.1	7.8	11	0.62-0.63				
4	GMAW	1	223-228	26.8-27.1	7.8	11	0.62-0.63				

Appendix I: Welding procedure specifications.

pre Welding Procedure Specification   pWPS

Parent material	SSAB Strenx 1100 MC Plus		
Material thickness	8 mm	Joint type	Welding sequences
Outside diameter	-		
Welding process	GMAW		
Welding position	2F		
Groove preparation	-		
Groove cleaning	Wire brush		
Workpiece fixturing	Clamped		
Tack welding	3 tack welds on the sides		
Back gouging	No		
Backing	No		

	Designation of consumables and trade name	Torch angle	45 deg
Filler material classification	E131T15-M21A4-K4-H4	Inclination angle	5 deg
	T89 4 ZMn2NiCrMo M M21 1 H5	Distance contact tube to workpiece	18 mm
	TZ834T15-1M21A-N4C1M2-UH5	Preheating and interpass temperature	
Filler material trade name	Bohler X96 L-MC	Preheat temperature	No (ambient)
		Interpass temperature	-
Flux	-	Preheating method	Ambient air
Shielding gas	Argon + 8 % CO$_2$	Temperature measurement	Pyrometer
Flow rate	14 l/min	Post-weld heat treatment	
Plasma gas	-	Method	-
Flow rate	-	Heating rate	-
Backing gas	-	Temperature	-
Flow rate	-	Time	-
Type of current	DC+	Cooling rate	-
Polarity		Post-weld treatment	Hiflt, HFMI treatment
Remarks:		Date and name:	

Run	Process	Size of filler metal Ø (mm)	Current (A)	Voltage (V)	Travel speed (mm/min)	Wire feed rate (m/min)	Heat input (kJ/mm)	Run-out length (mm)	Weaving frequency (Hz)	Amplitude (mm)	Remarks
1	GMAW	1	220-225	25.5-25.9	7.8	11	0.58-0.63				
2	GMAW	1	220-225	25.5-25.9	7.8	11	0.58-0.63				
3	GMAW	1	220-225	25.5-25.9	7.8	11	0.58-0.63				
4	GMAW	1	220-225	25.5-25.9	7.8	11	0.58-0.63				

Appendix II: Welding parameters

Specimen ID and pass	Current I [A]	Voltage U [V]	Travel speed v [mm/s]	wire feed rate[m/s]	Heat input Q [kJ/mm]	Cooling rate $t_{8/5}$, 2D [s]
S7_LNLC_1_1	214	26.1	7.8	11	0.57	3.90
ID2	213	26.2	7.8	11	0.57	3.90
ID3	220	25.9	7.8	11	0.58	4.06
ID4	220	26.2	7.8	11	0.59	4.16
S7_LNLC_1_2	217	26	7.8	11	0.58	3.98
ID2	217	26	7.8	11	0.58	3.98
ID3	221	25.8	7.8	11	0.58	4.07
ID4	222	25.9	7.8	11	0.59	4.14
S7_LNLC_1_3	214	26	7.8	11	0.57	3.87
ID2	218	26	7.8	11	0.58	4.02
ID3	221	25.8	7.8	11	0.58	4.07
ID4	226	25.7	7.8	11	0.60	4.22
S7_LNLC_1_4	217	26	7.8	11	0.58	3.98
ID2	219	26	7.8	11	0.58	4.06
ID3	219	25.9	7.8	11	0.58	4.03
ID4	224	25.8	7.8	11	0.59	4.18
S7_LNLC_1_5	217	26	7.8	11	0.58	3.98
ID2	220	25.9	7.8	11	0.58	4.06
ID3	219	25.9	7.8	11	0.58	4.03
ID4	220	25.8	7.8	11	0.58	4.03
S7_LNLC_1_6	215	26.1	7.8	11	0.58	3.94
ID2	221	26	7.8	11	0.59	4.13
ID3	218	26	7.8	11	0.58	4.02
ID4	225	25.7	7.8	11	0.59	4.18
S7_LNLC_1_7	215	26	7.8	11	0.57	3.91
ID2	218	25.9	7.8	11	0.58	3.99
ID3	224	25.8	7.8	11	0.59	4.18
ID4	225	25.8	7.8	11	0.60	4.22
S7_LNLC_1_8	220	27	7.8	11	0.61	4.42
ID2	222	25.9	7.8	11	0.59	4.14
ID3	219	25.9	7.8	11	0.58	4.03
ID4	228	25.8	7.8	11	0.60	4.33
S7_LNLC_1_9	222	25.9	7.8	11	0.59	4.14
ID2	221	26	7.8	11	0.59	4.13
ID3	219	25.9	7.8	11	0.58	4.03
ID4	220	25.9	7.8	11	0.58	4.06
S7_LNLC_1_10	221	26	7.8	11	0.59	4.13
ID2	221	26	7.8	11	0.59	4.13
ID3	218	25.9	7.8	11	0.58	3.99

Appendix II: Welding parameters.

Specimen ID and pass	Current I [A]	Voltage U [V]	Travel speed v [mm/s]	wire feed rate[m/s]	Heat input Q [kJ/mm]	Cooling rate $t_{8/5}$, 2D [s]
ID4	222	25.9	7.8	11	0.59	4.14
S7_LNLC_1_11	219	27	7.8	11	0.61	4.38
ID2	222	25.9	7.8	11	0.59	4.14
ID3	222	25.8	7.8	11	0.59	4.11
ID4	222	25.9	7.8	11	0.59	4.14
S7_LNLC_1_12	217	25.9	7.8	11	0.58	3.95
ID2	217	26	7.8	11	0.58	3.98
ID3	221	25.8	7.8	11	0.58	4.07
ID4	224	25.8	7.8	11	0.59	4.18
S7_LNLC_1_13	228	25.8	7.8	11	0.60	4.33
ID 2	224	25.9	7.8	11	0.60	4.21
ID 3	222	25.9	7.8	11	0.59	4.14
ID 4	223	25.9	7.8	11	0.59	4.17
S7_LNLC_1_14	222	25.9	7.8	11	0.59	4.14
ID 2	224	26	7.8	11	0.60	4.24
ID 3	225	25.8	7.8	11	0.60	4.22
ID 4	221	25.9	7.8	11	0.59	4.10
S7_LNLC_1_15	222	26	7.8	11	0.59	4.17
ID 2	223	26	7.8	11	0.59	4.21
ID 3	226	26	7.8	11	0.60	4.32
ID 4	223	25.7	7.8	11	0.59	4.11
S7_LNLC_1_16	223	25.9	7.8	11	0.59	4.17
ID 2	224	25.9	7.8	11	0.60	4.21
ID 3	222	26.1	7.8	11	0.59	4.20
ID 4	222	26	7.8	11	0.59	4.17
S7_LNLC_1_17	221	26	7.8	11	0.59	4.13
ID 2	223	26	7.8	11	0.59	4.21
ID 3	223	26	7.8	11	0.59	4.21
ID 4	224	25.9	7.8	11	0.60	4.21
S7_LNLC_1_18	220	26	7.8	11	0.59	4.09
ID 2	219	26.1	7.8	11	0.59	4.09
ID 3	224	25.9	7.8	11	0.60	4.21
ID 4	226	25.9	7.8	11	0.60	4.29
S1_LNLC_1	224	25.8	7.8	11	0.59	4.18
ID 2	224	25.6	7.8	11	0.59	4.12
ID 3	224	25.5	7.8	11	0.59	4.08
ID 4	222	25.6	7.8	11	0.58	4.04
S1_LNLC_2	224	25.7	7.8	11	0.59	4.15
ID 2	223	25.7	7.8	11	0.59	4.11
ID 3	222	25.7	7.8	11	0.59	4.07

Appendix II: Welding parameters.

Specimen ID and pass	Current I [A]	Voltage U [V]	Travel speed v [mm/s]	wire feed rate[m/s]	Heat input Q [kJ/mm]	Cooling rate $t_{8/5}$, 2D [s]
ID 4	225	25.6	7.8	11	0.59	4.15
S1_LNLC_3	222	25.8	7.8	11	0.59	4.11
ID 2	225	25.7	7.8	11	0.59	4.18
ID 3	222	25.6	7.8	11	0.58	4.04
ID 4	222	25.9	7.8	11	0.59	4.14
S1_LNLC_4	220	25.8	7.8	11	0.58	4.03
ID 2	224	25.6	7.8	11	0.59	4.12
ID 3	222	25.8	7.8	11	0.59	4.11
ID 4	222	25.7	7.8	11	0.59	4.07
S1_LNLC_5	222	25.9	7.8	11	0.59	4.14
ID 2	224	25.7	7.8	11	0.59	4.15
ID 3	220	25.7	7.8	11	0.58	4.00
ID 4	224	25.7	7.8	11	0.59	4.15
S1_LNLC_6	224	25.7	7.8	11	0.59	4.15
ID 2	224	25.7	7.8	11	0.59	4.15
ID 3	222	25.6	7.8	11	0.58	4.04
ID 4	224	25.7	7.8	11	0.59	4.15
S1_LNLC_7	224	25.7	7.8	11	0.59	4.15
ID 2	224	25.7	7.8	11	0.59	4.15
ID 3	223	25.7	7.8	11	0.59	4.11
ID 4	220	25.8	7.8	11	0.58	4.03
S1_LNLC_8	224	25.7	7.8	11	0.59	4.15
ID 2	224	25.7	7.8	11	0.59	4.15
ID 3	223	25.8	7.8	11	0.59	4.14
ID 4	221	25.6	7.8	11	0.58	4.01
S3_LNLC_1	226	27	7.8	11	0.63	4.66
ID 2	227	26.9	7.8	11	0.63	4.67
ID 3	227	26.8	7.8	11	0.62	4.63
ID 4	227	26.8	7.8	11	0.62	4.63
S3_LNLC_2	223	27.1	7.8	11	0.62	4.57
ID 2	227	26.9	7.8	11	0.63	4.67
ID 3	227	26.8	7.8	11	0.62	4.63
ID 4	228	26.8	7.8	11	0.63	4.67
S3_LNLC_3	226	27	7.8	11	0.63	4.66
ID 2	228	26.9	7.8	11	0.63	4.71
ID 3	228	26.8	7.8	11	0.63	4.67
ID 4	225	26.9	7.8	11	0.62	4.58
S3_LNLC_4	225	27.1	7.8	11	0.63	4.65
ID 2	226	26.9	7.8	11	0.62	4.63

Appendix II: Welding parameters.

Specimen ID and pass	Current I [A]	Voltage U [V]	Travel speed v [mm/s]	wire feed rate[m/s]	Heat input Q [kJ/mm]	Cooling rate $t_{8/5}$, 2D [s]
ID 3	228	26.9	7.8	11	0.63	4.71
ID 4	227	26.9	7.8	11	0.63	4.67
S3_LNLC_5	225	27.1	7.8	11	0.63	4.65
ID 2	228	26.9	7.8	11	0.63	4.71
ID 3	226	26.9	7.8	11	0.62	4.63
ID 4	223	26.9	7.8	11	0.62	4.50
S3_LNLC_6	225	27.1	7.8	11	0.63	4.65
ID 2	225	27	7.8	11	0.62	4.62
ID 3	228	26.9	7.8	11	0.63	4.71
ID 4	224	27	7.8	11	0.62	4.58
S3_LNLC_7	224	27.1	7.8	11	0.62	4.61
ID 2	225	26.9	7.8	11	0.62	4.58
ID 3	225	27	7.8	11	0.62	4.62
ID 4	226	26.9	7.8	11	0.62	4.63
S3_LNLC_8	223	27	7.8	11	0.62	4.54
ID 2	226	27	7.8	11	0.63	4.66
ID 3	224	27	7.8	11	0.62	4.58
ID 4	226	26.9	7.8	11	0.62	4.63
S7_LNLC_2_1	227	25.7	7.8	11	0.60	4.26
ID2	220	25.7	7.8	11	0.58	4.00
ID3	221	25.9	7.8	11	0.59	4.10
ID4	220	25.9	7.8	11	0.58	4.06
S7_LNLC_2_2	223	25.9	7.8	11	0.59	4.17
ID2	220	25.9	7.8	11	0.58	4.06
ID3	225	25.7	7.8	11	0.59	4.18
ID4	220	25.9	7.8	11	0.58	4.06
S7_LNLC_2_3	223	25.8	7.8	11	0.59	4.14
ID2	220	25.9	7.8	11	0.58	4.06
ID3	225	25.7	7.8	11	0.59	4.18
ID4	225	25.8	7.8	11	0.59	4.22

Appendix III: Complete test matrixes and fatigue test results.

Test matrix for S700 steel grade.

Specimen	Joint type	Welding process	Overload	Stress range	R	N_f
S7_LNLC_1_1	LNLC	GMAW	-	125	0.1	Runout
S7_LNLC_1_2	LNLC	GMAW	-	225	0.1	87928
S7_LNLC_1_3	LNLC	GMAW	-	155	0.1	5E6
S7_LNLC_1_4	LNLC	GMAW	-	200	0.1	119229
S7_LNLC_1_5	LNLC	GMAW	-	180	0.1	176984
S7_LNLC_1_6	LNLC	GMAW	-	170	0.1	201383
S7_LNLC_1_7	LNLC	GMAW	0.8	215	0.1	408661
S7_LNLC_1_8	LNLC	GMAW	0.8	225	0.1	668832
S7_LNLC_1_9	LNLC	GMAW	0.8	225	0.1	408737
S7_LNLC_1_10	LNLC	GMAW	0.8	250	0.1	202651
S7_LNLC_1_11	LNLC	GMAW	0.8	250	0.1	222192
S7_LNLC_1_12	LNLC	GMAW	0.8	215	0.1	382475
S7_LNLC_2_1	LNLC	GMAW	0.8	200	0.1	520000
S7_LNLC_1_13	LNLC	GMAW	0.6	225	0.1	122158
S7_LNLC_1_14	LNLC	GMAW	0.6	225	0.1	124437
S7_LNLC_1_15	LNLC	GMAW	0.6	200	0.1	177143
S7_LNLC_1_16	LNLC	GMAW	0.6	200	0.1	305230
S7_LNLC_1_17	LNLC	GMAW	0.6	250	0.1	201433
S7_LNLC_1_18	LNLC	GMAW	0.6	250	0.1	94939
S7_LNLC_2_2	LNLC	GMAW	-	VA1	0.05	313456
S7_LNLC_2_3	LNLC	GMAW	-	VA2	0.05	290000
S7_LNLC_2_4	LNLC	GMAW	-	VA3	0.05	130000
S7_LNLC_2_5	LNLC	GMAW	-	VA4	0.05	420000

Appendix III: Complete test matrixes for experimental fatigue tests

Test matrix for S355 steel grade.

Specimen	Joint type	Welding process	Stress range	R	N_f
S3_LNLC_1	LNLC	GMAW	225	0.1	97835
S3_LNLC_2	LNLC	GMAW	225	0.1	162375
S3_LNLC_3	LNLC	GMAW	OL1 + 225	0.1	123502
S3_LNLC_4	LNLC	GMAW	OL1 + 180	0.1	257206
S3_LNLC_5	LNLC	GMAW	OL1 + 180	0.1	237970
S3_LNLC_6	LNLC	GMAW	OL1 + 170	0.1	333116
S3_LNLC_7	LNLC	GMAW	OL1 + 160	0.1	451055
S3_LNLC_8	LNLC	GMAW	OL1 + 225	0.1	144596

Test matrix for S1100 steel grade.

Specimen	Joint type	Welding process	Stress range	R	N_f
S1_LNLC_1	LNLC	GMAW	OL1 + 250	0.1	$2.5E10^6$
S1_LNLC_2	LNLC	GMAW	OL1 + 350	0.1	82825
S1_LNLC_3	LNLC	GMAW	OL1 + 350	0.1	84410
S1_LNLC_4	LNLC	GMAW	OL1 + 325	0.1	219362
S1_LNLC_5	LNLC	GMAW	OL1 + 300	0.1	334752
S1_LNLC_6	LNLC	GMAW	OL1 + 280	0.1	835979
S1_LNLC_7	LNLC	GMAW	225	0.1	175667
S1_LNLC_8	LNLC	GMAW	225	0.1	167397

Appendix IV: Measured strains and degrees of bending

ID	$\Delta\mu\varepsilon$ [-]	σ_{sg} [MPa]	K_{hs}	$\Delta\sigma_{(nom)}$ [MPa]	σ_{hs} [MPa]	σ_b [MPa]	DOB [%]
S7_LNLC_1_1	830	174.3	1.423	125	177.875	-3.575	-2.05106
S7_LNLC_1_2	1641	344.61	1.423	225	320.175	24.435	7.090624
S7_LNLC_1_3	1058	222.18	1.423	155	220.565	1.615	0.726888
S7_LNLC_1_4	1435	301.35	1.423	200	284.6	16.75	5.558321
S7_LNLC_1_5	1377	289.17	1.423	180	256.14	33.03	11.42235
S7_LNLC_1_6	1283	269.43	1.423	170	241.91	27.52	10.21416
S7_LNLC_1_7	1390	291.9	1.423	215	305.945	-14.045	-4.81158
S7_LNLC_1_8	1449	304.29	1.423	225	320.175	-15.885	-5.22035
S7_LNLC_1_9	1424	299.04	1.423	225	320.175	-21.135	-7.06762
S7_LNLC_1_10	1734	364.14	1.423	250	355.75	8.39	2.304059
S7_LNLC_1_11	1574	330.54	1.423	250	355.75	-25.21	-7.62691
S7_LNLC_1_12	1595	334.95	1.423	215	305.945	29.005	8.659501
S7_LNLC_1_13	1538	322.98	1.423	225	320.175	2.805	0.868475
S7_LNLC_1_14	1568	329.28	1.423	225	320.175	9.105	2.765124
S7_LNLC_1_15	1456	305.76	1.423	200	284.6	21.16	6.92046
S7_LNLC_1_16	1284	269.64	1.423	200	284.6	-14.96	-5.54814
S7_LNLC_1_17	1637	343.77	1.423	250	355.75	-11.98	-3.48489
S7_LNLC_1_18	1850	388.5	1.423	250	355.75	32.75	8.429858
S7_LNLC_2_1	1497	314.37	1.423	200	284.6	29.77	9.469733
S1_LNLC_1	1831	384.51	1.423	250	355.75	28.76	7.479649
S1_LNLC_2	2412	506.52	1.423	350	498.05	8.47	1.672195
S1_LNLC_3	2490	522.9	1.423	350	498.05	24.85	4.752343
S1_LNLC_4	2292	481.32	1.423	325	462.475	18.845	3.915275
S1_LNLC_5	2126	446.46	1.423	300	426.9	19.56	4.381132
S1_LNLC_6	1942	407.82	1.423	280	398.44	9.38	2.300034
S1_LNLC_7	1635	343.35	1.423	225	320.175	23.175	6.749672
S1_LNLC_8	1511	317.31	1.423	225	320.175	-2.865	-0.9029
S3_LNLC_1	1699.35	356.8635	1.423	225	320.175	36.6885	10.28082
S3_LNLC_2	1533	321.93	1.423	225	320.175	1.755	0.54515
S3_LNLC_3	1722	361.62	1.423	225	320.175	41.445	11.46093
S3_LNLC_4	1388	291.48	1.423	180	256.14	35.34	12.12433
S3_LNLC_5	1325	278.25	1.423	180	256.14	22.11	7.946092
S3_LNLC_6	1322	277.62	1.423	170	241.91	35.71	12.86291
S3_LNLC_7	1212	254.52	1.423	160	227.68	26.84	10.54534
S3_LNLC_8	1550	325.5	1.423	225	320.175	5.325	1.635945

Appendix V: Residual stress measurements of steel grade S700.

S7_LNLC_1_12 before OL1					
Distance from the weld toe [mm]	**σ [MPa]: 0.0°**	**(±)**	**FWHM(°): 0.0°**	**(±)_1**	**2θ: 0.0°**
0	132.2	63.5	2.06	0.04	156.18
0.5	197.3	69.7	2.09	0.03	156.18
1	218.6	71.2	2.11	0.03	156.18
1.5	248	67.3	2.12	0.05	156.19
2	267.1	65.9	2.12	0.05	156.13
2.5	261.2	66.6	2.08	0.03	156.11
3	267.1	61.7	2.08	0.02	156.13
4	264.6	72.3	2.07	0.03	156.18
6	293.6	71.4	2.08	0.03	156.22
8	271	75.7	2.04	0.02	156.2
10	214.2	81.5	2.04	0.03	156.15

S7_LNLC_1_12 after OL1					
Distance from the weld toe [mm]	**σ [MPa]: 0.0°**	**(±)**	**FWHM(°): 0.0°**	**(±)_1**	**2θ: 0.0°**
0	-147.2	67.9	2.1	0.06	155.96
0.5	-74.8	92.3	2.17	0.05	156.04
1	-39	96.3	2.2	0.04	156.07
1.5	-49.3	95.6	2.2	0.03	156.07
2	-29.5	90.1	2.21	0.01	156.04
2.5	-56.1	99.5	2.22	0.02	156.02
3	-44.7	101.4	2.21	0.02	156.02
4	-45.1	88.7	2.22	0.04	156.1
6	-35.5	78.4	2.21	0.02	156.12
8	-21.3	81.1	2.18	0.03	156.12
10	-30.4	74.7	2.1	0.02	156.08

Appendix V: Residual stress measurements of steel grade S700.

S7_LNLC_1_17 before OL2					
Distance from the weld toe [mm]	σ [MPa]: 0.0°	(±)	FWHM(°): 0.0°	(±)_1	2θ: 0.0°
0	166.7	73.2	2.05	0.05	156.19
0.5	213.6	82.7	2.09	0.04	156.16
1	194.6	76.9	2.08	0.03	156.13
1.5	224.7	73.7	2.1	0.04	156.14
2	253.4	79.6	2.14	0.04	156.16
2.5	255.6	80.8	2.12	0.03	156.13
3	238.9	79.5	2.09	0.02	156.12
4	254.6	79	2.04	0.03	156.2
6	287.9	85	2.16	0.03	156.14
8	221.7	79	2.04	0.04	156.17
10	210	76	2.02	0.03	156.18

S7_LNLC_1_17 after OL2					
Distance from the weld toe [mm]	σ [MPa]: 0.0°	(±)	FWHM(°): 0.0°	(±)_1	2θ: 0.0°
0	-98.8	60.6	2.01	0.06	156
0.5	31.2	62.5	2.1	0.04	156.13
1	110.5	65.3	2.12	0.04	156.2
1.5	152.3	73.5	2.14	0.05	156.21
2	148.6	80.6	2.25	0.06	156.2
2.5	122.6	88.4	2.22	0.04	156.21
3	118	80.8	2.19	0.03	156.16
4	142.7	85.5	2.15	0.02	156.24
6	114.9	69.1	2.15	0.04	156.2
8	104.6	76.6	2.05	0.04	156.14
10	53.4	76.3	2.02	0.02	156.09

Appendix V: Residual stress measurements of steel grade S700.

S7_LNLC_2_1 As-welded					
Distance from the weld toe [mm]	σ [MPa]: 0.0°	(±)	FWHM(°): 0.0°	(±)_1	2θ: 0.0°
0	653.9	68.7	2.32	0.01	156.57
0.5	609.1	55.2	2.3	0.03	156.53
1	526.7	59.7	2.23	0.01	156.49
1.5	454.5	56.2	2.22	0.02	156.37
2	372.9	49.6	2.21	0.03	156.33
2.5	360.8	49.5	2.17	0.01	156.29
3	380.4	49.8	2.14	0.03	156.29
4	337.7	57.1	2.12	0.03	156.23
6	323.2	48.5	2.08	0.04	156.21
8	315.9	46.8	2.12	0.03	156.23
10	276.7	48.1	2.05	0.04	156.17

S7_LNLC_2_1 After HFMI treatment on the opposite side of the weld toe					
Distance from the weld toe [mm]	σ [MPa]: 0.0°	(±)	FWHM(°): 0.0°	(±)_1	2θ: 0.0°
0	252.2	62	2.25	0.06	156.19
0.5	336.5	46.7	2.24	0.03	156.21
1	369.4	44.9	2.24	0.02	156.19
1.5	345.5	53.5	2.2	0.02	156.2
2	311.9	49	2.19	0.04	156.15
2.5	331.6	48.8	2.2	0.03	156.19
3	380.3	43.5	2.17	0.03	156.22
4	378.3	47	2.14	0.02	156.2
6	390.9	45.8	2.1	0.02	156.21
8	352.5	29.4	2.09	0.02	156.21
10	297.4	35.4	2.05	0.02	156.17

Appendix V: Residual stress measurements of steel grade S700.

S7_LNLC_2_1 After OL1					
Distance from the weld toe [mm]	σ [MPa]: 0.0°	(±)	FWHM(°): 0.0°	(±)_1	2θ: 0.0°
0	-174	81.9	2.27	0.12	155.96
0.5	-100.4	76.8	2.36	0.03	156.08
1	-37.8	93.1	2.35	0.03	156.04
1.5	-62.3	103.6	2.33	0.04	156.09
2	-59.6	96.4	2.33	0.04	156.08
2.5	-51.2	88.2	2.34	0.04	156.1
3	-56.7	88.2	2.32	0.03	156.08
4	-48	90.5	2.31	0.03	156.12
6	-24.3	83.1	2.24	0.02	156.13
8	-13.9	78.7	2.21	0.03	156.11
10	-12.4	82.1	2.1	0.03	156.05

Appendix VI: Polished cross-sections and macro figures with hardness measurements

Appendix VI: Polished cross-sections and macro figures with hardness measurements